



**TALLINN UNIVERSITY OF TECHNOLOGY**  
SCHOOL OF ENGINEERING  
Department of Civil Engineering and Architecture

# **ANALYSIS AND MODELLING OF FIRE TESTS WITH I-JOISTS**

## **PUIDUST I-TALADEGA TULEKATSETE ANALÜÜS JA MODELLEERIMINE**

MASTER THESIS

Üliõpilane: Carmen Karma

Üliõpilaskood: 182213EAEI

Juhendaja: Katrin Nele Mäger  
doktorant-nooremteadur

Kaasjuhendaja: Professor Alar Just

Tallinn 2023

(Tiitellehe pöördel)

## **AUTORIDEKLARATSIOON**

Olen koostanud lõputöö iseseisvalt.

Lõputöö alusel ei ole varem kutse- või teaduskraadi või inseneridiplomit taotletud.

Kõik töö koostamisel kasutatud teiste autorite tööd, olulised seisukohad,

kirjandusallikatest ja mujalt pärinevad andmed on viidatud.

"....." ..... 201.....

Autor: .....

/ allkiri /

Töö vastab bakalaureusetöö/magistritööle esitatud nõuetele

"....." ..... 201.....

Juhendaja: .....

/ allkiri /

Kaitsmisele lubatud

"....." .....201... .

Kaitsmiskomisjoni esimees .....

/ nimi ja allkiri /

## **Lihtlitsents lõputöö reprodutseerimiseks ja lõputöö üldsusele kättesaadavaks tegemiseks<sup>1</sup>**

Mina, Carmen Karma, (sünnikuupäev: 04.06.1999)

1. Annan Tallinna Tehnikaülikoolile tasuta loa (lihtlitsentsi) enda loodud teose „I-taladega kandekonstruktsioonide tules käitumise modelleerimine“, mille juhendaja on Katrin Nele Mäger,
  - 1.1 reprodutseerimiseks lõputöö säilitamise ja elektroonse avaldamise eesmärgil, sh Tallinna Tehnikaülikooli raamatukogu digikogusse lisamise eesmärgil kuni autoriõiguse kehtivuse tähtaja lõppemiseni;
  - 1.2 üldsusele kättesaadavaks tegemiseks Tallinna Tehnikaülikooli veebikeskkonna kaudu, sealhulgas Tallinna Tehnikaülikooli raamatukogu digikogu kaudu kuni autoriõiguse kehtivuse tähtaja lõppemiseni.
2. Olen teadlik, et käesoleva lihtlitsentsi punktis 1 nimetatud õigused jäävad alles ka autorile.
3. Kinnitan, et lihtlitsentsi andmisega ei rikuta teiste isikute intellektuaalomandi ega isikuandmete kaitse seadusest ning muudest õigusaktidest tulenevaid õigusi.

---

<sup>1</sup>*Lihtlitsents ei kehti juurdepääsupiirangu kehtivuse ajal, välja arvatud ülikooli õigus lõputööd reprodutseerida üksnes säilitamise eesmärgil.*

\_\_\_\_\_ (allkiri)

\_\_\_\_\_ (kuupäev)

**TTÜ Ehituse ja arhitektuuri instituut**  
**LÕPUTÖÖ ÜLESANNE**

**Üliõpilane:** Carmen Karma 182213EAEI  
**Õppekava, peeriala:** EAEI02/17 – Ehitiste projekteerimine ja ehitusjuhtimine  
**Juhendaja:** Katrin Nele Mäger, Alar Just

**Lõputöö teema:**

Puidust I-taladega tulekatsete analüüs ja modelleerimine.

Analysis and modelling of fire tests with I-joists.

**Lõputöö põhieesmärgid:**

1. I-taladest konstruktsioonide tules käitumise termiline simuleerimine
2. Ettepanekud arvutusmudeli muutmiseks

**Lõputöö etapid ja ajakava:**

<b>Nr</b>	<b>Ülesande kirjeldus</b>	<b>Tähtaeg</b>
1.	Kirjanduse analüüs	
2.	Katseraportite analüüs	
3.	Modelleeritavate konstruktsioonide ja parameetrite valik	
4.	Termilised simulatsioonid	
5.	Tulemuste võrdlus katseandmetega	
6.	Analüüs ja järeldused	
7.	Töö vormistamine	

**Töö keel:** inglise

**Lõputöö esitamise tähtaeg:** "22" mai 2023.a

**Üliõpilane:** Carmen Karma ..... ".....".....202....a  
/signature/

**Juhendaja:** Katrin Nele Mäger ..... "....."..... 202....a  
/signature/

# CONTENTS

PREFACE.....	6
LIST OF ABBREVIATIONS AND SYMBOLS.....	7
1. INTRODUCTION.....	8
2. BACKGROUND.....	10
2.1 I-joists.....	10
2.2 Problems.....	11
2.3 Fire design models.....	13
2.3.1 Rectangular members.....	14
2.3.2 I-shaped members.....	16
3. MATERIALS AND METHODS.....	20
3.1 Loaded model scale tests.....	20
3.2 Thermal simulations.....	22
4. RESULTS.....	24
4.1 Tests.....	24
4.2 Simulations.....	27
4.2.1 Recalibration of plasterboard data.....	28
4.2.2 Comparison between original and modified plasterboard data.....	29
5. ANALYSIS AND DISCUSSION.....	34
5.1 Residual cross-sections of fire exposed flanges.....	36
5.2 Cross-section comparison tables.....	41
5.3 Results and discussion.....	47
SUMMARY.....	50
KOKKUVÕTE.....	51
LIST OF REFERENCES.....	52

## **PREFACE**

I would like to take this opportunity to express my sincere appreciation to the individuals and institutions that have played a vital role in enabling the completion of this work.

My co-supervisor, Alar Just, proposed the subject of this thesis. The specimens were constructed and tested at RISE Fire Research in Trondheim, using wood supplied by Moelven Limtre AS.

I would like to extend my gratitude to all those who have supported me during my academic journey. I am particularly grateful to my supervisor, Katrin Nele Mäger, for her unwavering encouragement and guidance. Her consistent and constructive feedback throughout the entire work process has been immensely valuable to me.

Keywords: I-joist, fire design, charring, bending capacity, fire tests

# LIST OF ABBREVIATIONS AND SYMBOLS

## Latin lower case letters

$b$	width of the initial cross-section
$b_{ef}$	width of the effective cross-section
$b_{f1,1}$	width of the fire exposed flange of an I-joist for the fire situation
$b_n$	notional width of the cross-section
$b_w$	initial cross-section width of the web
$d_0$	zero-strength layer depth
$d_{char,n}$	notional charring depth
$d_{char,1,n}$	notional charring depth at fire exposed side
$d_{char,2,n}$	notional charring depth at lateral side
$d_{char,w}$	notional charring depth of the web
$h$	height of the initial cross-section
$h_{ef}$	height of the effective cross-section
$h_{f1,1}$	height of the fire exposed flange of an I-joist for the fire situation
$t$	time of fire exposure
$t_{ch}$	start time of charring on the fire exposed side
$t_{ch,w}$	start time of charring of the web
$t_{ch,2}$	start time of charring on the lateral side

## Greek upper case letters

$\Pi k_i$	product of applicable modification factors for charring
-----------	---

## Greek lower case letters

$\beta_0$	basic design charring rate
$\beta_n$	notional design charring rate within one charring phase

# 1. INTRODUCTION

Timber buildings are becoming more popular in construction due to their sustainability, efficiency, and aesthetic appeal. Different types of wooden materials, such as cross-laminated timber (CLT), glue laminated timber (glulam), and laminated veneer lumber (LVL), are engineered to provide the necessary strength for tall buildings. One advantage of tall wooden buildings is their low carbon footprint compared to traditional construction materials. Prefabrication methods allow for quick and efficient construction, reducing construction time and costs.

I-joists are a type of engineered wood product used in modern constructions for floors, walls, and roofs. They are a viable alternative to traditional wooden frames because of their advantages, flexibility, and demonstrated structural reliability. I-joists have flanges positioned at both the top and bottom with web material in between them. They are lightweight, straight, and have a high load-bearing capacity relative to their weight. I-joists are eco-friendly and energy-efficient, with less material required compared to conventional wooden frames.

Fire safety is a concern with larger and taller timber buildings, and there is currently no universal method for calculating the fire resistance of load-bearing timber frame structures with wooden I-joists. Analytical calculations and experimental fire testing are the two options to assess fire resistance. Full-scale fire tests are very accurate but at the same time require a lot of resources and time.

The thesis consists of four main parts, the first provides an overview of various timber constructions, along with their advantages and disadvantages. It also includes an explanation of different existing models describing I-joist constructions. The second part analyses the conducted loaded model scale tests. Thirdly, the thermal simulations carried out during the work are explained. In the fourth part, the results of the experiments are compared with the results obtained from simulations. Final conclusions are made based on the results of the entire work.

The objective of this thesis is to investigate and analyse the fire behaviour of I-joists through finite element thermal simulations and fire test results. The goal of this research is to calculate the zero-strength layer depths based on fire test data. Further, thermal properties of protection materials (gypsum) were calibrated in order to achieve a high level of similarity between the results of simulations and tests. During the thermal simulations conducted for this study, the author considered not only the I-joist itself but also the existing fire protection system (such as gypsum board and cavity insulation)

and the timing of plasterboard fall-off. Temperatures and charred cross-sections were compared from tests and simulations. In addition, the zero-strength layer corresponding to each tested I-joist will be determined as a result of cross-section measurements and various calculations.

## **2. BACKGROUND**

Timber buildings are gaining popularity in the construction industry due to their sustainability, efficiency and appearance. There are various types of wooden buildings, such as cross-laminated timber (CLT), glue-laminated timber (glulam) and laminated veneer lumber (LVL). These materials are engineered to ensure the required strength and stability for constructing tall buildings.

One of the main advantages of tall wooden buildings is their low carbon footprint. Wood is a renewable resource, so it has a much lower environmental impact than traditional building materials like concrete and steel. Additionally, timber buildings can be constructed quickly and efficiently using prefabrication methods, reducing construction time and costs.

### **2.1 I-joists**

The I-joist is a type of engineered wood product that finds use in various constructions and buildings. Owing to its numerous advantages, flexibility, and demonstrated structural reliability, the I-joist has emerged as a viable alternative in modern wooden constructions, serving as a load-bearing element in floors, walls, and roofs.

I-joists are used as load-bearing frame materials in the construction element system, they are typically combined with board material, insulation and membranes to provide moisture barrier and air sealing properties while also enhancing fire safety, acoustics and stability.

There are three building systems available for using I-joists: on-site, construction elements and modules [1]. To select the most suitable building system, several factors must be taken into account, including the building's location, type, technical specifications and accessibility. The on-site building system involves assembling the building component by component at the site. In contrast, the construction element system comprises prefabricated elements, where different parts of the building are premanufactured either on site or in a factory. Finally, the volume or module building system involves creating the building in modules that are constructed off site and transported to the building site, where they are assembled using various components.

The I-joist derives its name from its resemblance to the letter "I," owing to its flanges positioned at both the top and bottom, with web material in between them. These flanges can be constructed using various grades of timber or LVL, while the web material is often composed of OSB, particleboard, plywood, or other materials like glass.

Masonite Beams specializes in manufacturing I-joists with construction-grade wooden flanges and a web composed of 10 mm OSB/3 or 10 mm particle board. [1]

Figure 2.1 displays the labels of the parts of an I-joist in the context of fire design.

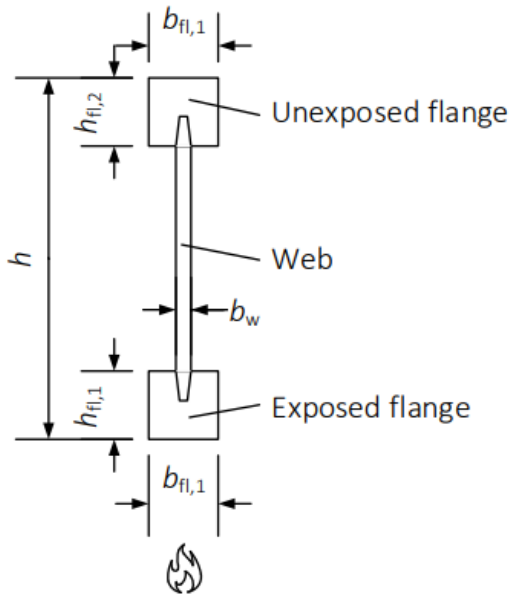


Figure 2.1. The naming of the parts of an I-joist. [2]

The general interest to use I-joints is increasing as the time goes on, as the buildings get higher and at the same time it is preferable to keep making more environmentally friendly choices. The advantages to using I-joints are their lightness, straightness and high load-bearing capacity relative to weight. In today's context where environmental regulations are becoming more stringent and heating costs are rising, it is crucial to choose construction materials that are both eco-friendly and energy efficient. I-joints stand out as a unique option due to their exceptional ability to use raw materials efficiently. As much as 80% of the wood's volume can be utilized, and less material is required compared to conventional wooden frames [1]. Additionally, the web of an I-joist is typically quite thin allowing for a reduction of thermal bridges when I-joints are used in external walls or roofs. Consequently, this leads to lower energy expenses and lower overall household costs.

## 2.2 Problems

The biggest concern when it comes to larger and taller timber buildings is often fire safety. Generally, there are two options to assess the fire resistance of a timber structure - analytical calculations based on approved design methods and experimental fire testing of a small section of the structure [3]. Calculation methods are the easiest,

fastest and most economical way to check if the fire resistance of a given structure meets the necessary requirements. Considering that I-joists are extremely optimised in their use of wood resources, they are also more sensitive to fire.

Currently there is no universal method for calculating the fire resistance of load-bearing timber frame structures with wooden I-joists, as the current European design standard for timber structures in fire - Eurocode 5 Part 1-2 (2004) provides no guidance for I-joists. Combining a new method that would cater the needs of market and engineers is however just a matter of time. Biggest issues and drawbacks of available methods are listed in articles written by Mäger. [3]

The alternative approach for ensuring the fire resistance of structures is through fire testing. While full-scale fire tests are highly accurate and dependable, they are resource-intensive and time-consuming. Additionally, the outcomes may only be relevant to the particular structure that was tested, and extrapolating the results or modifying the configuration of the structure may not be feasible. Furthermore, the test results are frequently kept confidential, leading to a variety of technical guidance documents and approved structures that are only applicable to specific products [3].

The strength of a timber member used in a timber frame assembly that supports weight is affected by pyrolysis, which occurs when wood is exposed to high temperatures. Although pyrolysis is often simplified as "charring" for structural applications, which is assumed to happen at 300 °C, there are additional stages in the pyrolysis process that can impact the load-bearing capacity of a timber member [4]. At temperatures below 200 °C, mass loss due to pyrolysis occurs slowly, with pyrolyzate consisting mainly of non-flammable volatiles such as carbon dioxide, formic acids, and acetic acids. However, prolonged heating at low temperatures can transform hemicellulose (and lignin) into a char at temperatures as low as 95 °C or 120 °C, leaving cellulose mostly unreacted. Although cellulosic materials do not have a fluid state, they may soften before breaking down into vapors, potentially undergoing a glass transition that alters their structure and makes them softer and more rubbery. This phenomenon occurs for lignin at temperatures ranging from 55 °C to 170 °C, with permanent reductions in timber strength being observed at temperatures as low as 65 °C. When the temperature surpasses 200 °C, the pyrolyzate remains primarily non-flammable, but visible discoloration will start or intensify, with prolonged exposure to these temperatures resulting in slow charring. In long fires, uncharred wood remains at moderate temperatures due to the high heat losses from the char layer. The primary pyrolysis reactions usually begin between 225 °C and 275 °C. [5]

## 2.3 Fire design models

The new Eurocode 5 standard draft provides the European charring model, which is a simplified model for calculating the residual cross-section, assuming a linear rate of charring at different charring phases.

The European charring model consists of multiple charring phases and should be considered where relevant [4]:

- **Normal charring phase (Phase 1)** for the initially unprotected sides of timber members,
- **Encapsulated phase (Phase 0)**, for initially protected sides of timber members where no charring occurs behind the fire protection system,
- **Protected charring phase (Phase 2)**, for initially protected sides of timber members where charring occurs behind the fire protection system while it remains in place,
- **Post-protected charring phase (Phase 3)**, for initially protected sides of timber members after the failure of the fire protection system but before a fully developed char layer has formed,
- **Consolidated charring phase (Phase 4)**, for initially protected sides of timber members with a fully developed char layer.

Each phase is defined by a time period that expresses the characteristic events in that phase.

The notional charring rate should be taken as constant with time or throughout a charring phase. The notional design charring depth is calculated according to the formula (2.1):

$$d_{\text{char},n} = \beta_n t \quad (2.1)$$

where  $d_{\text{char},n}$  – the notional charring depth, mm,

$\beta_n$  – the notional design charring rate, which includes the effect of corner roundings and fissures, mm/min,

$t$  – the time of fire exposure (or length of a charring phase), min. [4]

The notional design charring rate can be calculated with formula (2.2) [4] :

$$\beta_n = \prod \beta_0 k_i \quad (2.2)$$

where  $\beta_0$  – the basic design charring rate, mm/min,

$\prod k_i$  – the product of applicable modification factors for charring.

The most important fire barrier for timber frame assemblies is the cladding on the fire side [6]. The influence of fire on reducing the size and strength of the timber member will increase extensively after the fall-off of cladding. Cavity insulations can still provide some protection.

Insulation material has several other functions in addition to its primary purpose, such as offering support for a surface finish, hindering the transmission of water vapor, minimizing or preventing harm to equipment and structures from fire or freezing temperatures and decreasing noise and vibration levels [7].

Correct fixation of cladding and insulation, the quality of the adhesives used, location of knots, local defects and many more factors also play an important role in keeping the timber frame assemblies safe from fire [6].

Sometimes the rupture of the load bearing I-joist can be caused by the specific adhesive used. In a recent research project, different adhesives were compared during experiments [8]. During the tests it appeared that there were 3 groups of adhesives. The weaker ones that broke before charring had started, those that broke 8-10 minutes after charring had started and the strongest adhesives lasted above 30 minutes and failure was mainly caused by the timber reaching its maximum strength.

### **2.3.1 Rectangular members**

In his doctoral thesis, Mattia Tiso has proposed different protection levels of cavity insulations against the charring (from stronger to weaker) that are determined by the relevant model scale furnace test:

- PL1 - insulation materials which guarantee that 2/3 of the lateral side of the timber cross-section is protected against charring for 60 min (e.g. stone wool).
- PL2 - insulation materials which do not guarantee the complete protection of the sides of members for up to 60 min (e.g. glass wool, cellulose fibre).

- PL3 - insulation materials which allow charring on the sides of members cross-section during the protection phase (e.g. extruded polystyrene) [6].

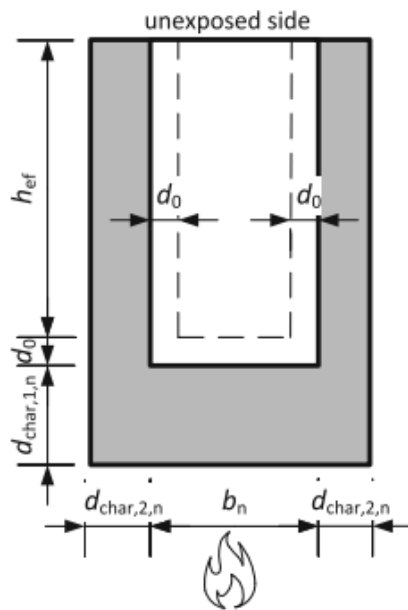


Figure 2.2. Principles of the new design model for a rectangular member [6].

Explanations of symbols shown in Figure 2.2:

$b_n$	notional width of the cross-section
$d_0$	zero-strength layer depth
$d_{char,1,n}$	notional charring depth at fire exposed side
$d_{char,2,n}$	notional charring depth at lateral side
$h_{ef}$	height of the effective cross-section

Timber elements with rectangular cross-sections have three distinct charring phases. The first phase, known as the encapsulation phase (Phase 1), refers to the period where no charring takes place. Phase 2 corresponds to the slow charring that occurs behind the protective panelling. Phase 3 signifies the rapid charring phase that follows the removal of protection. For visual representation see Figure 2.3.

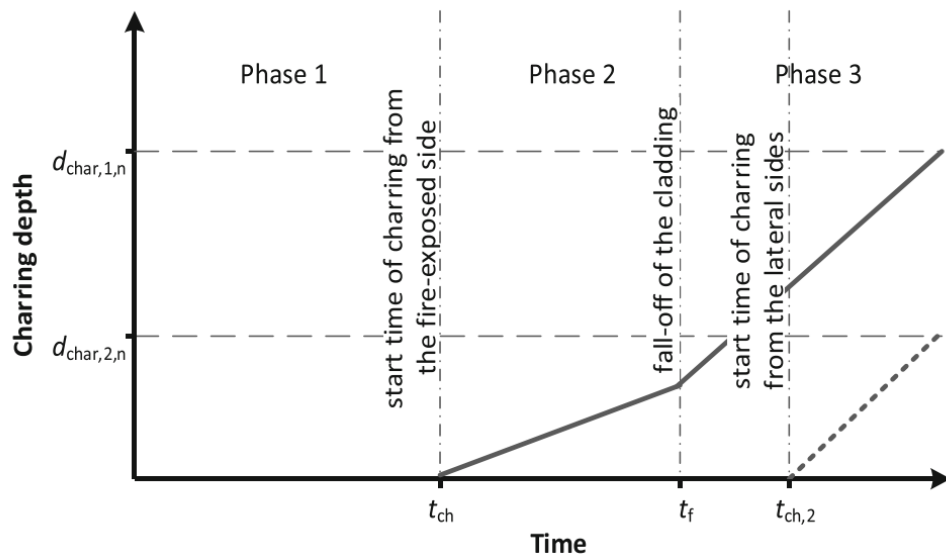


Figure 2.3. Charring phases for rectangular members [6].

When considering PL1 cavity insulation, charring needs to be taken into account solely on the fire-exposed side. In the case of PL3 cavity insulation, the initiation of charring on the fire-exposed side also determines the initiation of charring on the lateral sides.

The zero-strength layer is, in addition to the char layer, the thickness of the layer subtracted from the total cross-section to find the dimensions of the effective cross-section. The effective cross-section is assumed to have the strength and stiffness properties of timber at ambient temperatures. For a rectangular cross-section, see the location of  $d_0$  in Figure 2.2. When considering bending members, the thickness of the zero-strength layer varies significantly depending on factors such as geometry, the existence of protective cladding, and the duration of fire exposure. [9]

Although the zero-strength layer is not dependent on the charring rate, the depth of charring is crucial in determining the residual cross-section. Assuming an excessively large residual cross-section and a lower charring rate for determining the residual cross-section would lead to an increased value for the zero-strength layer. Conversely, assuming an overly small residual cross-section would result in a reduced thickness for the zero-strength layer. [9]

### 2.3.2 I-shaped members

The charring model developed by Mattia Tiso [7] for timber frame assemblies with rectangular cross-sections has been adapted to estimate the charring of wooden I-joists.

I-joists are particularly susceptible to charring due to their small cross-sectional area of the flanges, thin web, and the presence of adhesives. Therefore, the charring calculations proposed by Tiso have been adjusted to more accurately account for I-joists.

When dealing with wooden I-joists, there are typically four charring phases for the fire-exposed side of the flange. The charring phases are seen in Figure 2.4.

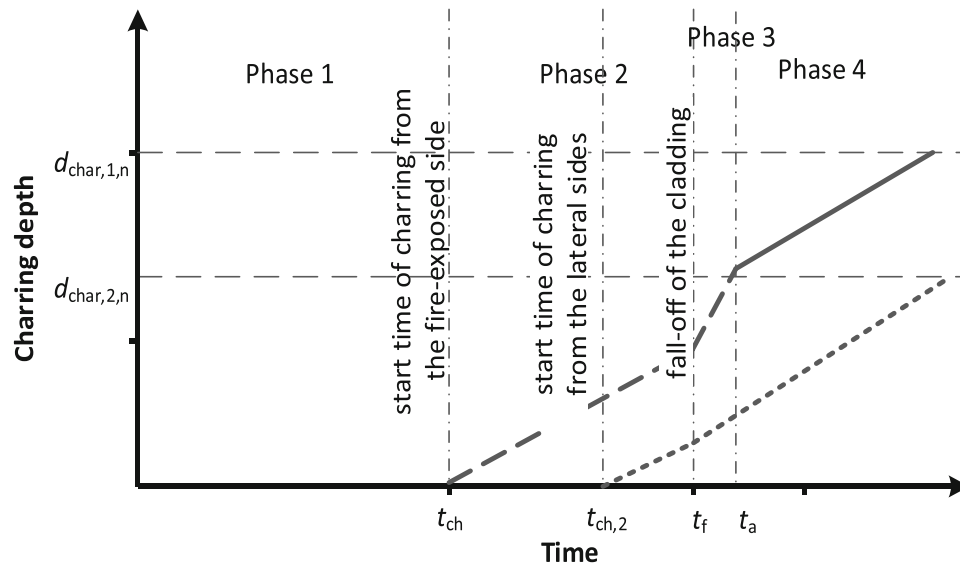


Figure 2.4. Charring phases for exposed flange of an I-joist [6].

I-joists may char on the fire exposed side of the exposed flange and on the lateral sides of the exposed flange. The start time of lateral charring ( $t_{ch,2}$ ) is considered as the time from the beginning of the fire exposure until the top corner (see point  $t_{ch,2}$  in Figure 2.5) reaches 300 °C. Charring may occur on the web. Start time of charring on the web is considered as the time to reach 300 °C at the point marked with  $t_{ch,w}$  in Figure 2.5. The principles of the design method for I-joists are shown in Figure 2.5.

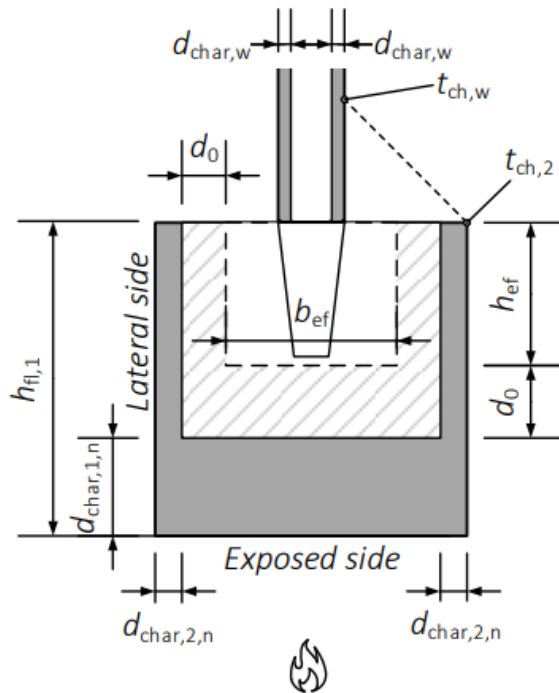


Figure 2.5. Principles of the new design mode for an I-joist [6].

Explanations of symbols shown in Figure 2.5:

$b_{ef}$	width of the effective cross-section
$d_0$	zero-strength layer depth
$d_{char,1,n}$	notional charring depth at fire exposed side
$d_{char,2,n}$	notional charring depth at lateral side
$d_{char,w}$	notional charring depth of the web
$h_{ef}$	height of the effective cross-section
$h_{fl,1}$	height of the cross-section of the timber member required for fire situation
$t_{ch,w}$	start time of charring of the web
$t_{ch,2}$	start time of charring on the lateral side

In the draft of the new Eurocode 5 standard [4], formulas are given in Table I.3, according to which maximum values of zero-strength layer depth for I-shaped members can be found. Zero-strength layer is subtracted from three sides of the fire exposed flange as shown in Figure 2.5.

The aim of this thesis is modelling fire behaviour of I-joists using finite element thermal simulations and comparing the results with test results. The desired outcome of this

work is for those results to be as similar as possible. In the performed thermal simulations the author of this thesis has taken into account in addition to the I-joist the existing fire protection system (gypsum board, cavity insulation) and the fall-off time of the plasterboard, so that the obtained results would be as similar as possible to the test results. A similar work was done by Mäger a few years prior [2]. Furthermore, the zero-strength layer for each beam will be calculated based on cross-section measurements.

## **3. MATERIALS AND METHODS**

Within this thesis thermal simulations and fire tests were investigated.

### **3.1 Loaded model scale tests**

Throughout the experiment a total of 14 tests were carried out, during which all the required test data was documented. The specimens for testing were constructed and tested at RISE Fire Research in Trondheim. Wood for the I-joists, which had been graded to class T22 with a density of 430-480 kg/m<sup>3</sup>, was supplied by Moelven Limtre AS.

Eleven adhesives were used in FIREWOOD project in order to compare their properties in fire. These adhesives were originated from four different chemical backgrounds, represented the state of the art of adhesives used in timber structures and were manufactured by four leading European adhesive manufacturers. All eleven adhesives have passed requirements in European standards for use in load-bearing timber structures. Adhesives were marked with numbers 1 to 12 (adhesive no 10 was not included in this Work Package). The adhesive numbers were similar in all tests throughout the project.

Blanks were glued with all 11 adhesives and then cut in half longitudinally. I-joists were produced with each half as the middle part of the tension flange. One of the I-joists in each pair was tested until rupture in bending tests at ambient temperature, while the other I-joist was tested in fire, with its strength predicted according to the trendline of relations between MOE and bending strength. The specimen length was 4.6 meters for all tests. The cavity insulation used was stone wool with a density of 30 kg/m<sup>3</sup>, and the fire-exposed side was covered with 15mm Type F gypsum board. The gypsum boards were connected to the assembly using steel elements at the edges, but were not fastened to the I-joist. The section of the specimen can be seen in Figure 3.1 and the test setup in Figure 3.2.

Type K thermocouples were used to measure temperatures in the assembly during the testing. The placement of the thermocouples is displayed in Figure 3.1. The thermocouple wires were stapled to the joists and guided towards the unexposed side.

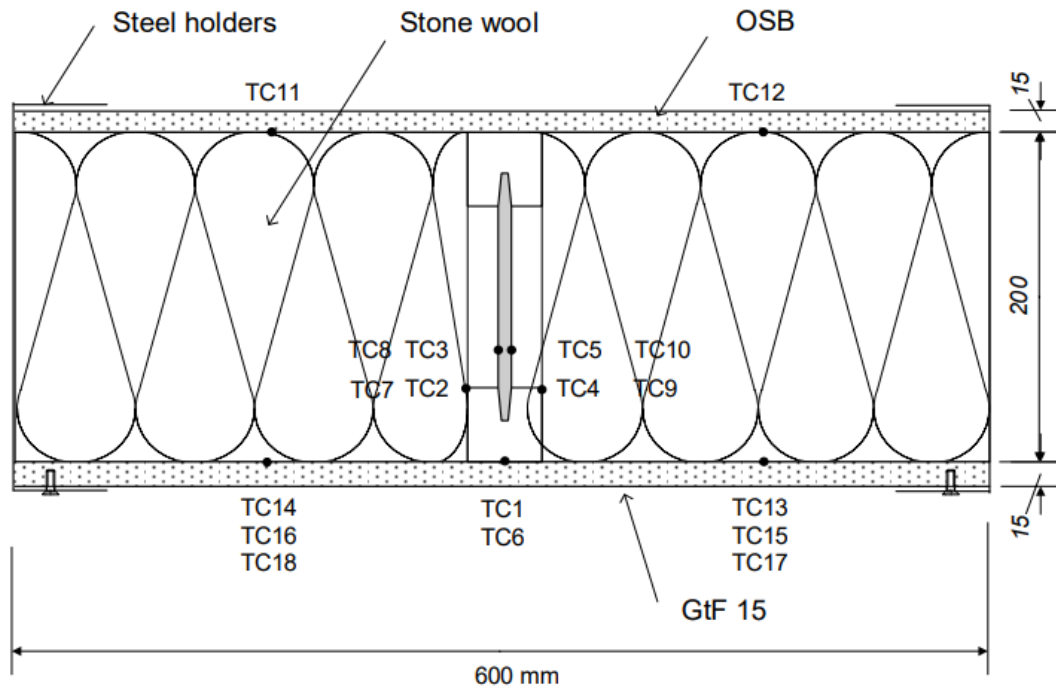


Figure 3.1. Section of the specimen. Location of thermocouples. [10]

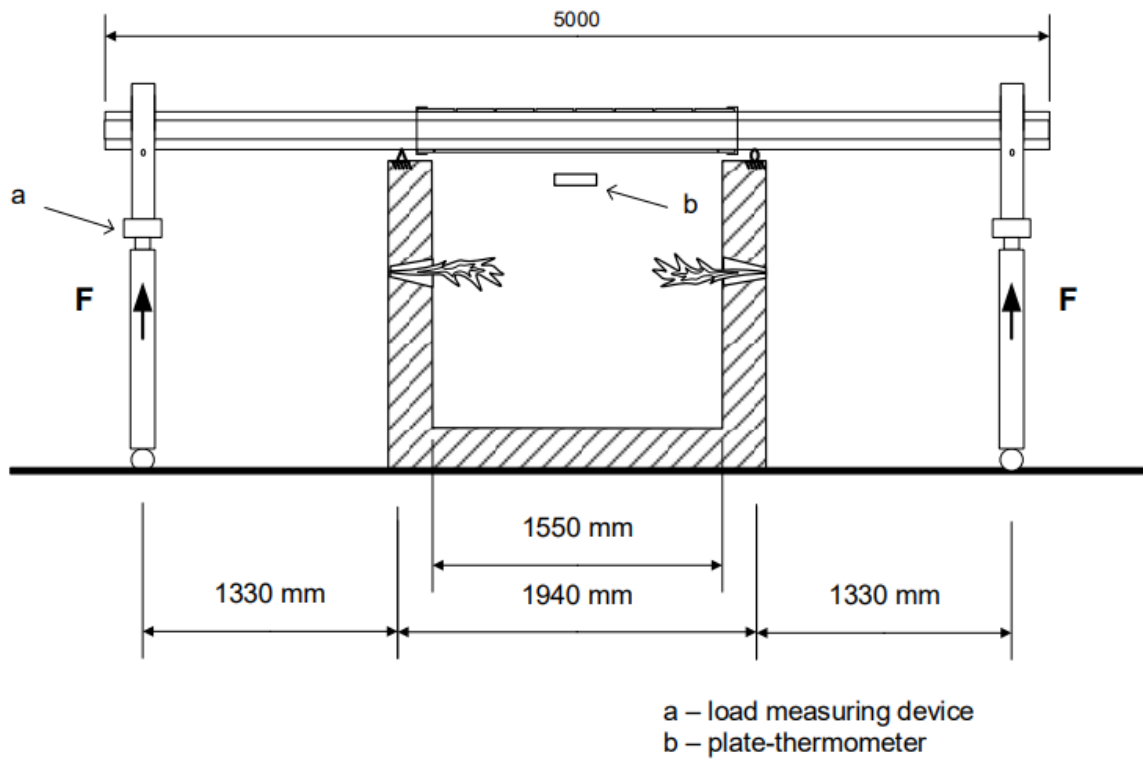


Figure 3.2. Test setup. [10]

## 3.2 Thermal simulations

Thermal finite element simulations were conducted using SAFIR software. [11], [12]

The simulated sections were divided into rectangular elements. The sizes of the elements were varied between 1x1 mm and 5x5 mm. The rectangular elements with a size of 1x1 mm were located on the fire exposed side of the I-joist, whereas on the opposite side, referred to as the "cold side", the size of the elements increased to 5x5 mm.

Differently sized elements are displayed in Figure 3.3. The time intervals were set at a maximum of 5 seconds. A simulation was performed on half of a frame assembly. Distance between the centres of the beams was 600 mm. The sides of the simulated structure were adiabatic surfaces.

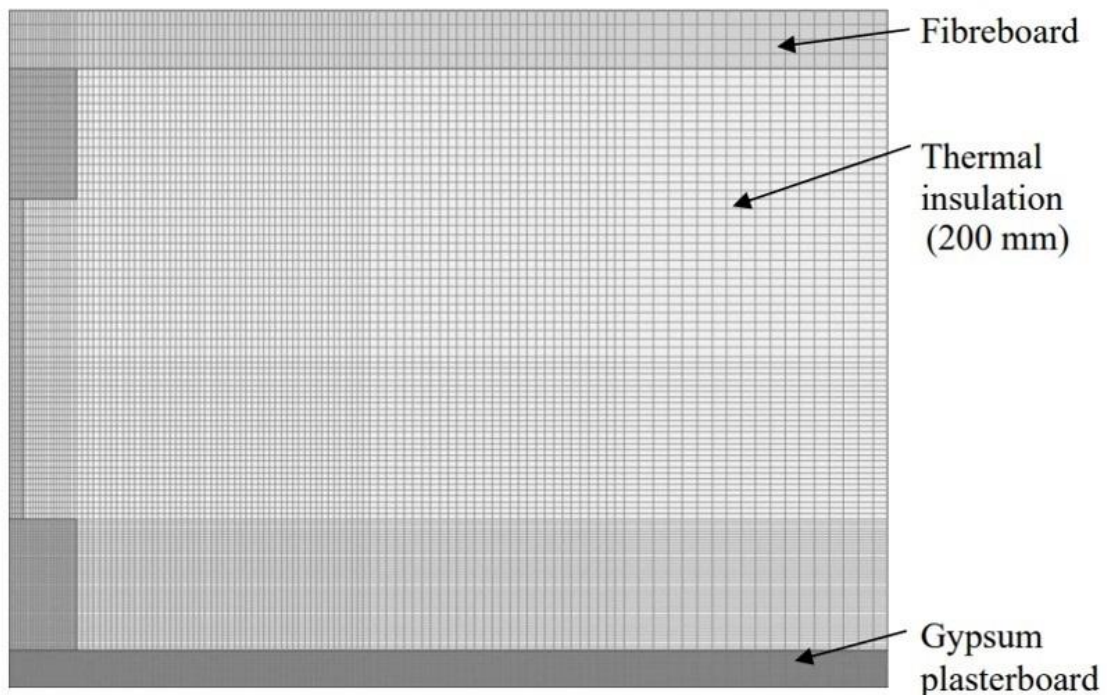


*Figure 3.3 Rectangular elements with varying sizes of simulated sections [light timber frames].*

All simulated I-joists had a height of 200 mm, the flange width and depth were both 47 mm. The specimens were protected by gypsum plasterboard, Type F (15 mm) on the fire exposed side. The unexposed side was covered by a 15 mm thick wooden fibreboard. The cavities were filled with stone wool insulation with a density of 26 kg/m<sup>3</sup>. A cross-section of the test specimen from the test report is shown in Figure 3.1.

Due to the fact that all the constructions' measurements were the same, two main base values needed from the test data table were the fall-off time of the fire protection system and test duration. The test duration was calculated by subtracting the test start time from test end time.

In order to get the necessary information for the fall-off, three thermocouples were picked from the total of 18, which were located right behind the fire protection gypsum board. All of the picked points located between the gypsum board and insulation. The failure time of gypsum plasterboard was considered to occur when the temperature jump was at least 20 degrees per second. The data of thermocouples that were numbered as 13, 14 and 18 were taken as a basis for finding the fall-off time. For all fourteen tests the test duration and fall-off time (if there was a gypsum board fall-off) were recorded.

The input file for the program SAFIR is a text file. For generating the input file, an Excel file was used when entering the required data for performing the simulations. Using the program Safir Shell, thermal simulations were performed, where the .IN files were converted to .OUT and .XML files. Fall-off of gypsum plasterboard was described by a second input file where the elements representing gypsum were removed. The simulation was continued from the fall-off time until the full duration of the fire test. The second simulation described thermal behaviour of the materials after the fall off.

After the first round of comparing simulation results with actual test results, it was clear, that the graphs were quite different. Starting with improving the simulations, three experiments were selected. Three experiments 6.3, 8.4 and 12.4, which had long protection phases, were taken as a basis. In order to get the results of the simulations as similar as possible to the real results, the thermal properties of the plasterboard were adjusted. Density and thermal conductivity were left unchanged. However, the heat capacity values were modified. The values were changed by observing five points for which temperatures were retrieved from both experiments and simulations throughout the entire test run. If, for the three selected beams, the temperature lines obtained were as close as possible to the real ones, the simulations of all other beams were also performed again with new data.

## 4. RESULTS

### 4.1 Tests

After conducting the tests, the cross-sections were cleaned of loose coal with a steel brush. All broken I-joists were then documented in full length and from the places where the breakage occurred. On the example of the beam 2.4, fracture images are presented in Figure 4.1 and Figure 4.2. About 5 cm long pieces were cut from the I-joists, perpendicular to the longitudinal axis of the I-beam, close to the breaking point. Both sides of these pieces were drawn on paper and scanned with a ruler next to them. At least two contour lines were scanned for each tested beam. The drawn cross-sections are seen in Figure 4.3.



*Figure 4.1. Broken I-joist 2.4 in full length.*



*Figure 4.2. Broken I-joist 2.4, position where the wood breakage took place.*

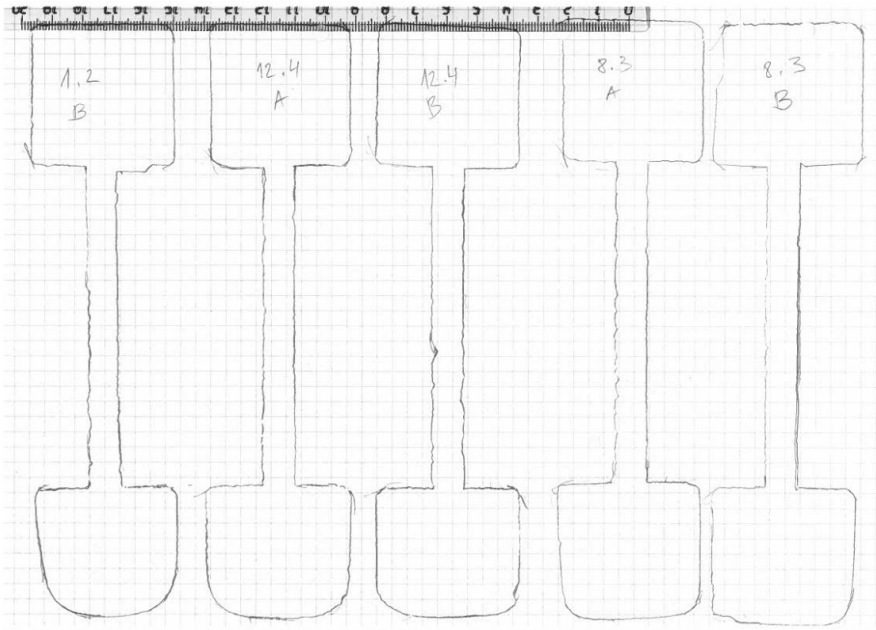


Figure 4.3. Contour lines of the scanned remaining cross-sections.

When the contours were redrawn in the AutoCAD program and were then ready for further use for all the I-joists, it was possible to find further necessary cross-section properties based on them. The redrawn contours are seen in Figure 4.4 using a few I-joists as an example.

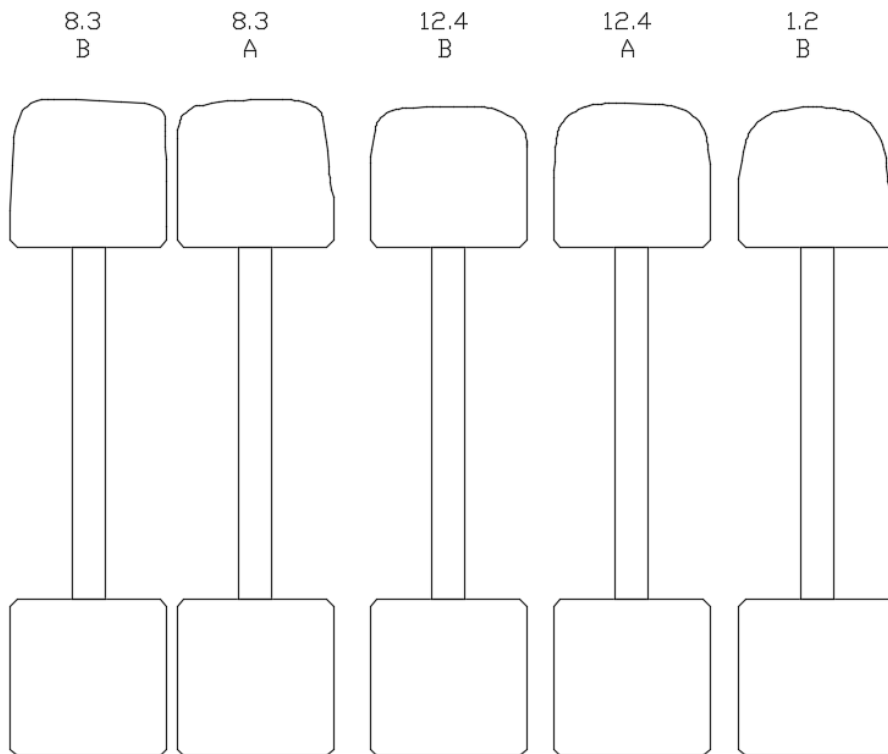


Figure 4.4. I-joist contours drawn based on the scans.

The charred cross-section contours were converted into closed polylines. The resulting contours were one by one moved to the starting point of the coordinates so that the centre under the cold flange was at the zero point. Further, it was possible to turn the polyline into a region, from which all the necessary cross-section properties could be retrieved with the command 'massprop'. As a result of this work, the cross-sectional area, the moment of inertia around the x-axis and the centroid in relation to the y-axis were obtained. The diagram showing the obtained contour and data output are shown in Figure 4.5 and Figure 4.6.

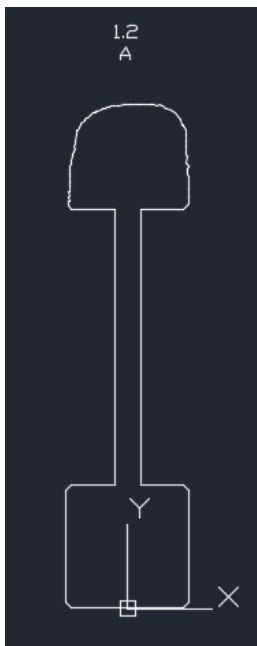


Figure 4.5. Contour of the cross-section of beam 1.2 at the origin of the coordinates.

```

----- REGIONS -----
Area:                4917.1224
Perimeter:           532.2730
Bounding box:        X: -23.5000 -- 23.5000
                    Y: 0.0000 -- 193.2638
Centroid:            X: 0.3245
                    Y: 89.8926
Moments of inertia:  X: 62214336.8172
                    Y: 664328.5402
Product of inertia:  XY: -285635.4105
Radii of gyration:   X: 112.4837
                    Y: 11.6235
Principal moments and X-Y directions about centroid:
                    I: 22481592.8290 along [1.0000 -0.0065]
                    J: 662884.0499 along [0.0065 1.0000]

```

Figure 4.6. Data output retrieved about the cross-section of the beam number 1.2.

Table 1 provides an overview of the timeline of all experiments.

*Table 1. Test summary data.*

Test beam	Test duration [min]	Fall-off time [min]	Start time of charring [min]	Start time of lateral charring [min]
2.2	26.4	-	20.3	-
8.3	26.08	-	19.7	-
6.3	38.78	-	20.9	-
5.2	11.85	-	-	-
9.2	24.07	-	21.1	-
4.3	22.6	-	19.0	-
11.2	12.23	11.65	-	-
12.4	32.38	-	21.2	-
2.4	29.7	19.77	17.5	27.8
7.4	15.2	-	-	-
1.2	24.33	20.33	17.8	-
3.3	29.33	19.85	19.0	23.5
11.4	29.42	-	20.5	-
8.4	36.82	-	19.3	-

## 4.2 Simulations

For comparing the actual test temperatures recorded by thermocouples with the ones from the simulations, five points were picked, where there had been thermocouples positioned during the tests. For the same points there was exported temperature data from all 14 simulations. The location of the points is seen in Figure 4.7.

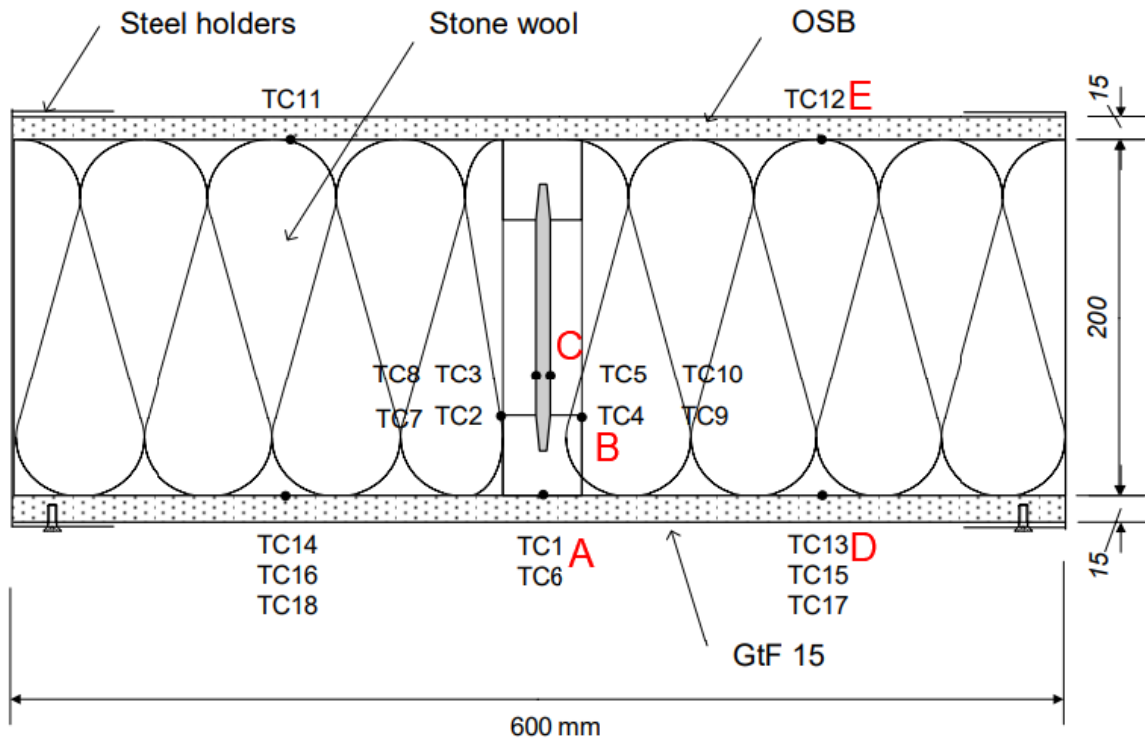


Figure 4.7. The location of the points A to E, where temperatures were compared.

#### 4.2.1 Recalibration of plasterboard data

When comparing the first simulation results with the actual test results, it became obvious that the graphs were significantly different. In order to get the results to be more similar to each other, the thermal properties of gypsum were recalibrated. A couple tests, where the fall-off time was long or did not occur during the test, were taken as a sample with a purpose to get results to be as similar as possible to test results. It is important to precisely observe those tests where the fall-off time is long or does not exist at all, because in such tests the impact of the plasterboard is the greatest on the course of the experiment.

In order to improve the similarities, the fire protection system parameters were modified by changing the values of gypsum plasterboard's specific heat capacity ( $c$ ). The comparison of the values originally stated in the guide and the updated values can be seen in Figure 4.8. The values taken from the guide "Fire safety in timber buildings" are marked as  $c_{\text{original}}$  and the changed new values as  $c_{\text{new}}$ . Other important gypsum plasterboard parameters needed for the simulations, like density and thermal conductivity, were taken from the guideline „Fire safety in timber buildings" [13].

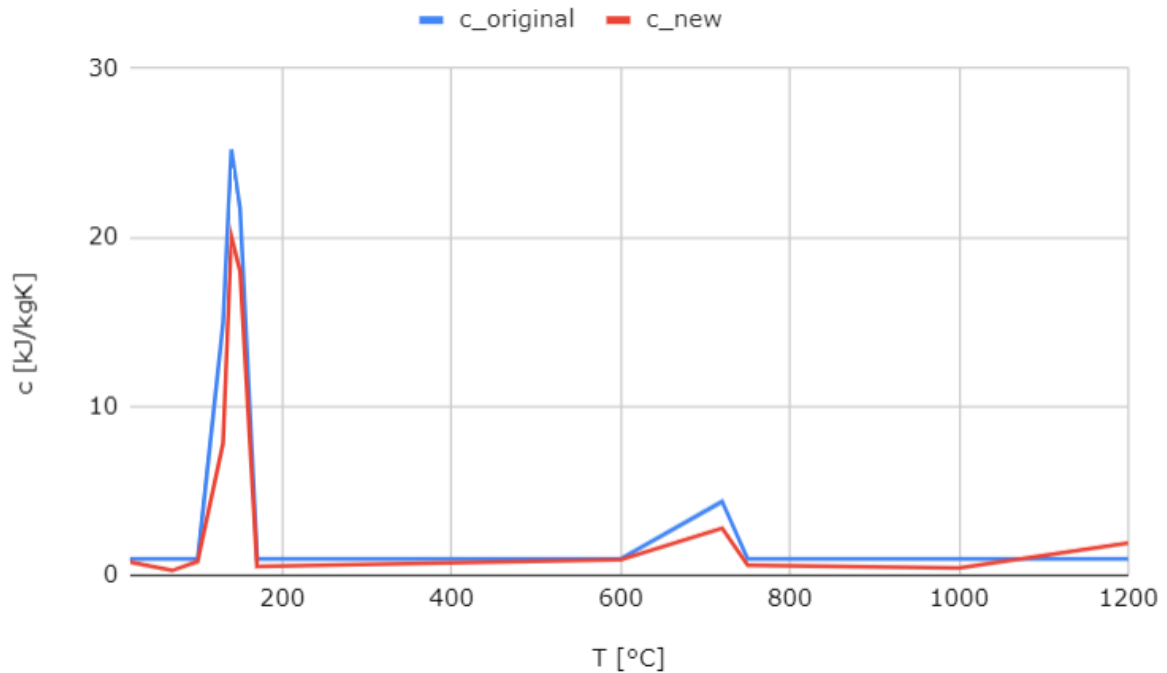


Figure 4.8. The comparison of values of specific heat capacity before and after recalibrating.

The plasterboard values were corrected based on the test beams 6.3, 8.4 and 12.4. Beam numbered as 6.3 had a long fall-off time, during the test with beam 8.4 the gypsum plasterboard fall-off did not occur, and in the experiment with beam 12.4 the plasterboard had a fairly short fall-off time.

After changing the data for the given beams, the temperature lines obtained were as close to the real ones as currently possible. Now, when the input parameters were established, all the simulations were redone.

#### 4.2.2 Comparison between original and modified plasterboard data

Next, the nature of the temperature lines obtained from the simulations will be compared with the original gypsum data and then with later changes.

For this, two beams are selected, with the results presented before and also after changing the plasterboard data:

- a test, where no gypsum plasterboard fall-off occurred – beam 11.4,
- a test with a gypsum plasterboard fall-off – beam 2.4.

Improvement of the results in the simulations after recalibrating the base values in the example of test beam 11.4 are shown in Figure 4.9 and Figure 4.10. In the test with beam 11.4, there was no gypsum plasterboard fall-off.

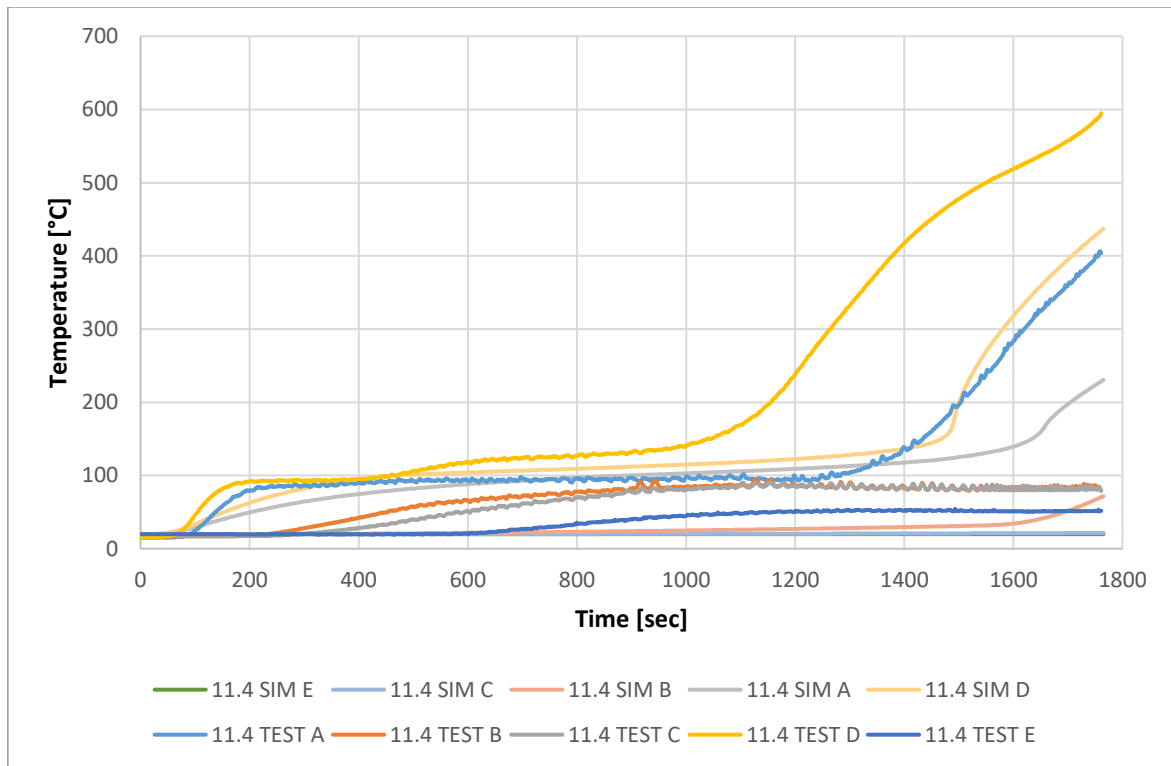


Figure 4.9 The comparison of simulation and test results of test beam 11.4 before recalibrating the base values.

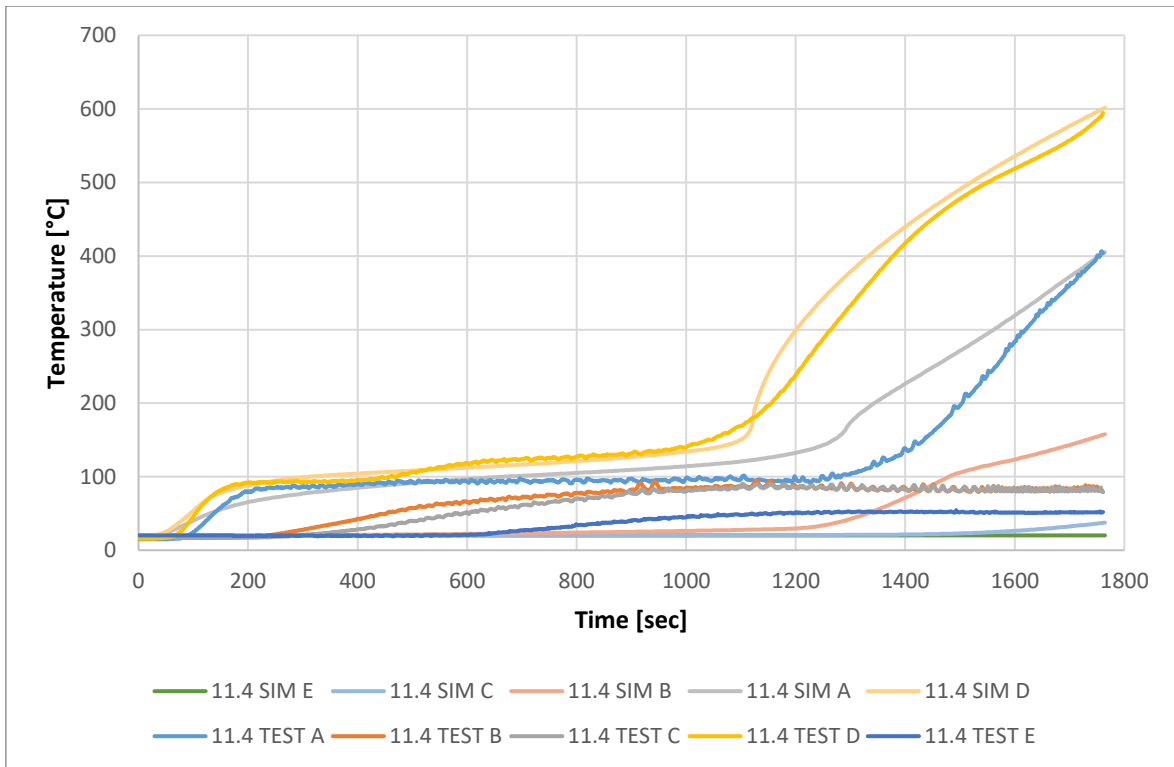


Figure 4.10. The comparison of simulation and test results of test beam 11.4 after recalibrating the base values.

After changing the characteristics of the gypsum plasterboard, the outcome was, that now the simulation results were on the „safe side“ of the chart compared to the actual test results. The notion that the simulation data is now "on the safe side" compared to the experimental results means that, to a large extent, the line of the simulated experiment either coincides with that of the experiment or describes the course of the experiment more conservatively than it actually occurred.

Looking at the differences in the temperature graphs in Figure 4.9 and Figure 4.10 of beam 11.4 before and after changing the data, it can be seen that after recalibrating the simulations describe the actual experiment much better than before. The highest temperatures occurred at point D. See Figure 4.7 for the location of the points. With the original data, the temperature line of the simulation at point D was much lower compared to that of the experiment. After the correction of the data, the lines almost overlap, and to a large extent the line of the simulation is located higher than the line from the actual experiment in terms of temperatures. The same can be noticed at point A, where changing the data completely changed the state of the graph, and the course of the experiment at this point can be safely described with the line obtained from the simulation. The temperature changes of the lower points were a little more minimal, but

it can also be said that the lines describing the temperature rise of the simulations and experiments are very similar.

Secondly a test beam will be observed, where the gypsum plasterboard fall-off occurred. For this, experiment performed with the beam 2.4 will be reviewed.

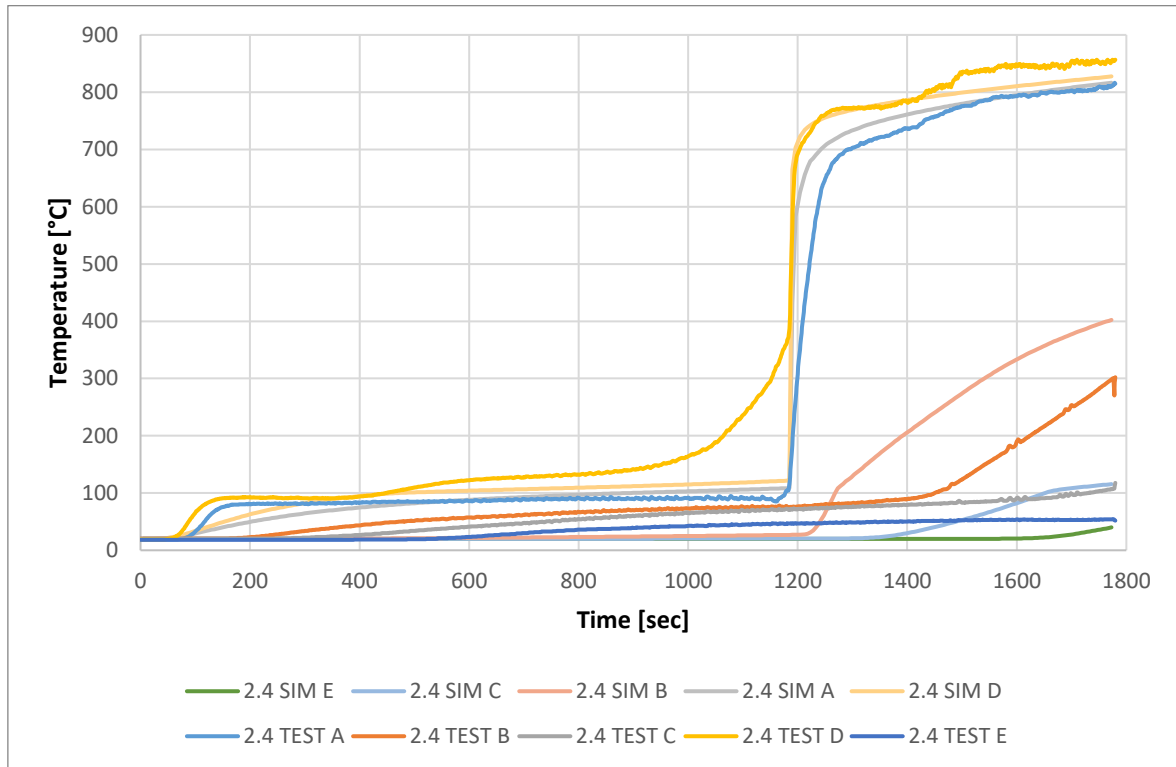


Figure 4.11. The comparison of simulation and test results of test beam 2.4 before recalibrating the base values.

Looking at the graph seen in Figure 4.11, when the plasterboard thermal properties had not been changed yet, it can be seen that the lines of simulations and experiments are located quite similarly when comparing the points A to E. At first, the temperature lines of the tests rise faster than those of the simulations. Also, in the time period 500-1000 seconds, the actual temperatures are higher than the ones obtained from the simulation. At 1200 seconds, the temperature lines of the simulations and test results largely overlap when viewing the points A and D. By the end of the experiment, both lines when viewing the point A are at a very similar height. Similarly, at lower temperatures, the lines of the simulations are on the safe side. At point D, however, the temperatures in the simulation do not rise as high as in the experiment.

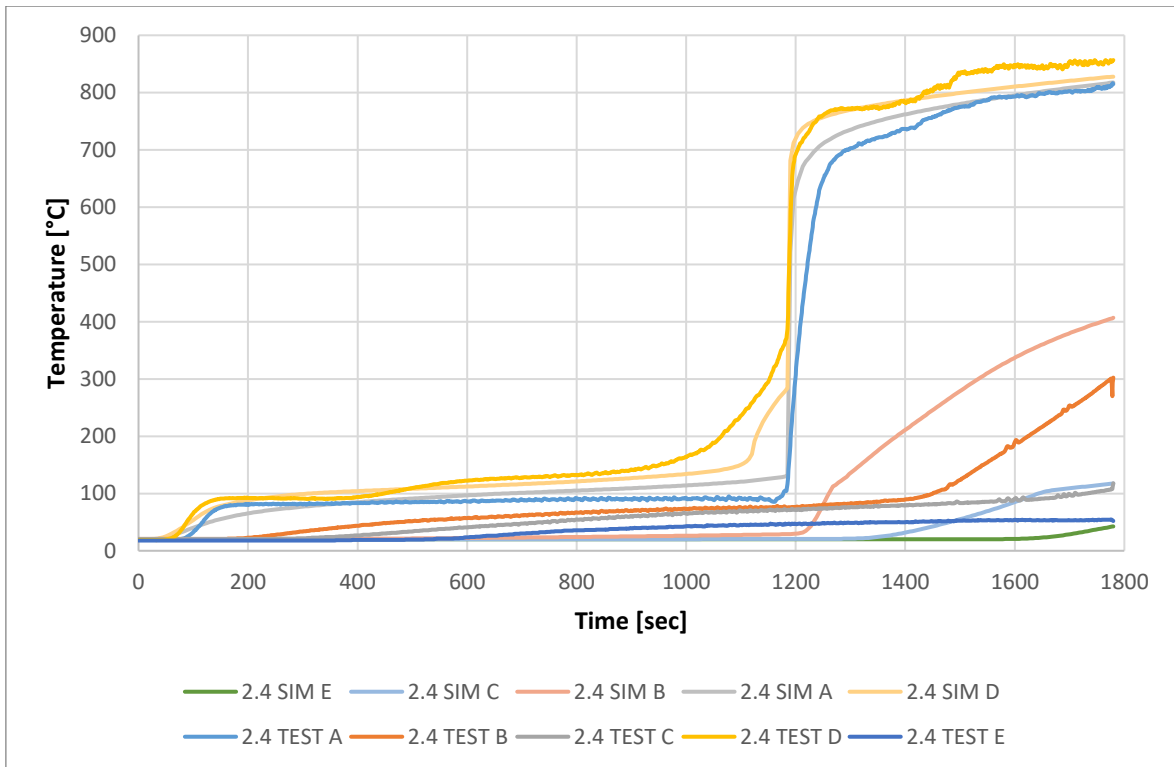


Figure 4.12. The comparison of simulation and test results of test beam 2.4 after recalibrating the base values.

From the graphs of the temperature of the beam 2.4, it can be seen that the test has a rather short fall-off time. Comparing the graphs seen in Figure 4.11 and Figure 4.12, it is seen that the temperature lines of the simulation have largely changed during the long fall-off time. It can be noticed that already at the beginning of the experiment, the temperature lines of the simulation and of the actual experiment are now much more similar. Comparing the temperatures, the rise of the lines at points A and D in the simulations are almost as steep as the lines of the actual results. If before changing the gypsum plasterboard data, the temperature lines of the test were quite different from those of the simulation in the period 500-1000 seconds, then after the change, the similarity is much greater. However, there is still room for improvement, so that the lines of the simulations would overlap those of the test or even better be on the safe side. Temperatures in the last few hundred seconds of the experiment were generally unchanged. At lower temperatures, the lines of the simulations are mostly on the safe side.

## 5. ANALYSIS AND DISCUSSION

Several types of breakage occurred in the tests. The main ones were the failure due to reaching the bearing capacity of the wood and the failure of the glue. In Figure 5.1 there is shown beam failure due to wood breakage. Adhesive failure can be seen, for example, in Figure 5.2.



*Figure 5.1. Failure due to reaching the bearing capacity in the example of beam 2.2.*



*Figure 5.2. Adhesive failure of a I-joist flange in the example of beam 4.3.*

Looking at the photos of the different test beams after testing, there is a noticeable trend that beams broken due to glue are noticeably less charred than those that failed due to wood breakage. Glues which soften at elevated temperatures lead to earlier loss of load-bearing capacity.

The various cross-sections, on which charring took place and from which it was possible to trace the outline of after testing, are shown in Figure 5.3. The following Figure 5.4 shows the theoretical cross-sections of the same I-joists in the same order.

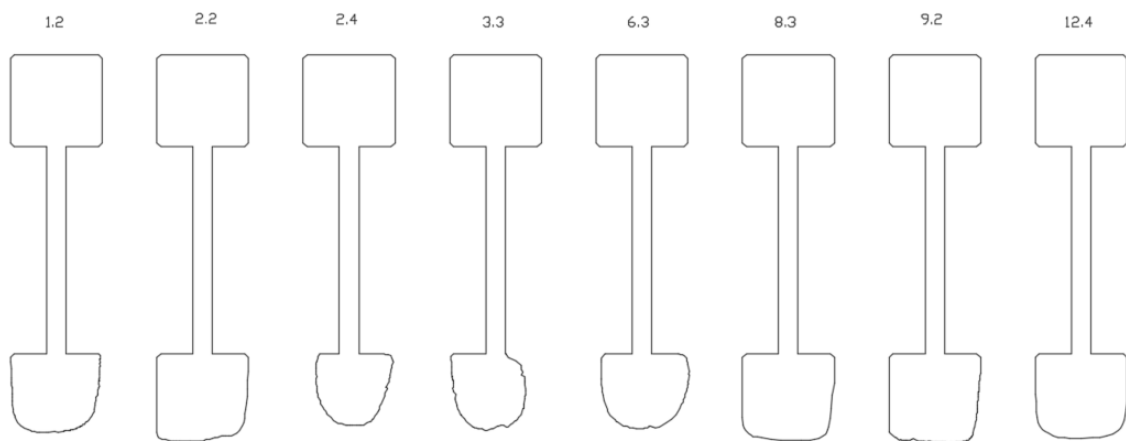


Figure 5.3. Actual I-joist contours from the tests performed.

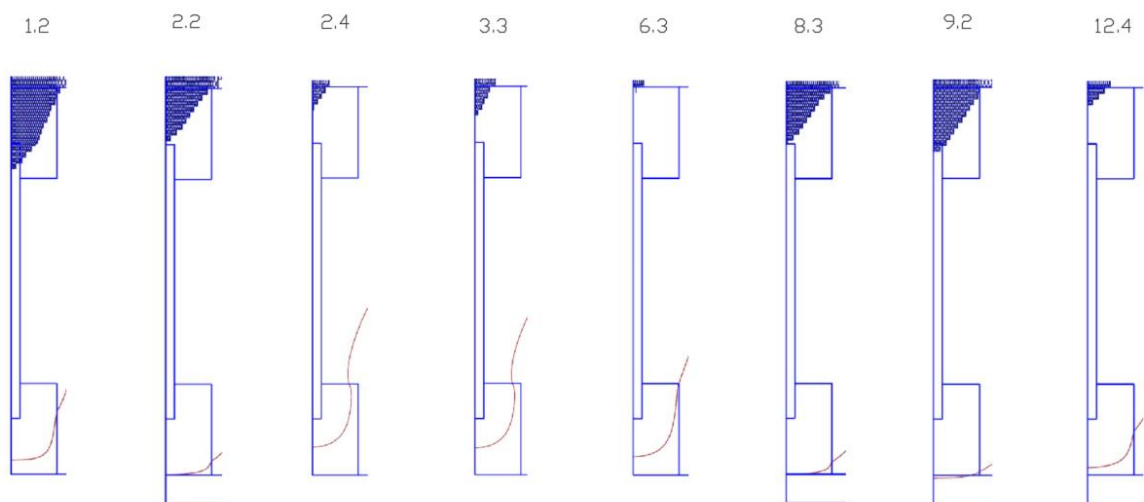


Figure 5.4. Cross-sections obtained from simulations with a marked charring line. Blue triangles on the top flange are visual noise from the post processor.

In order to better compare the fire exposed flanges, residual cross-sections created as a result of the simulations, which were obtained from the Diamond program, were also

drawn into the AutoCAD program. Afterwards it was possible to move the contours of the cross-sections from the actual tests and from the simulations on top of each other, which simplified the comparison of different contours. In the following, the fire exposed flanges are shown, with the fire exposed side on the bottom.

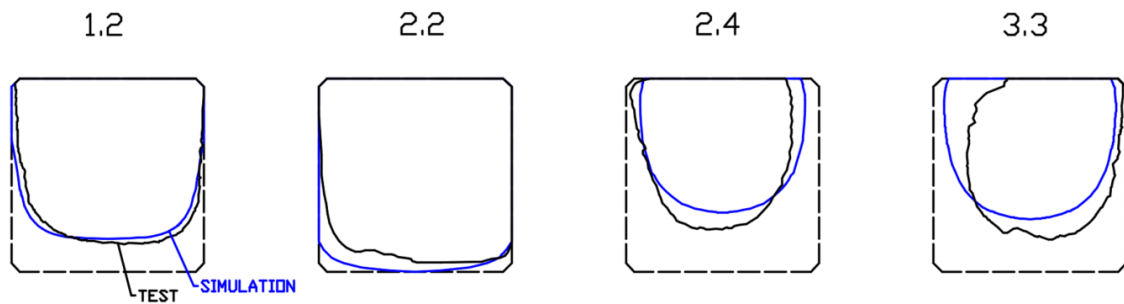


Figure 5.5. The comparison of measured and simulated residual cross-sections for the beams 1.2, 2.2, 2.4 and 3.3.

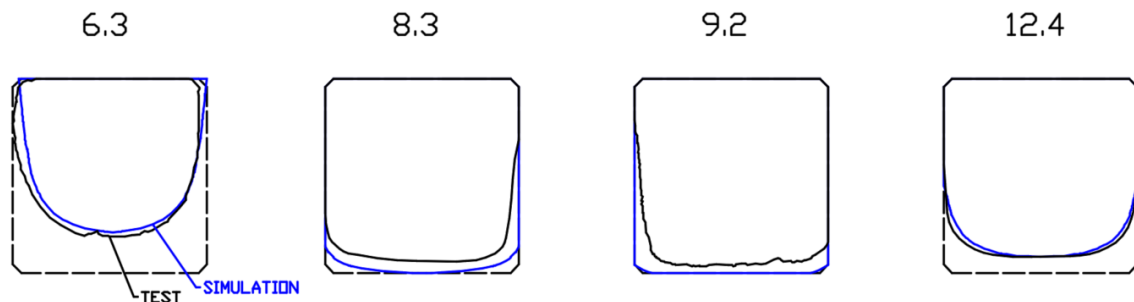
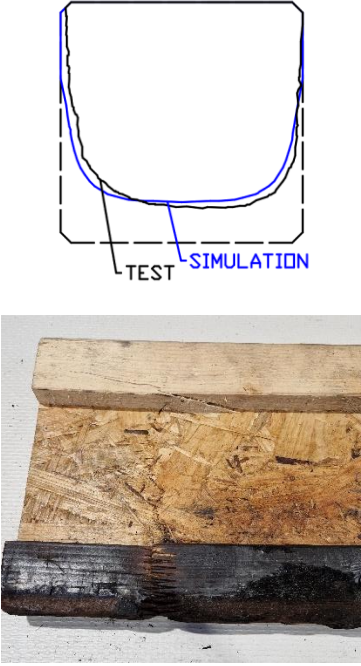
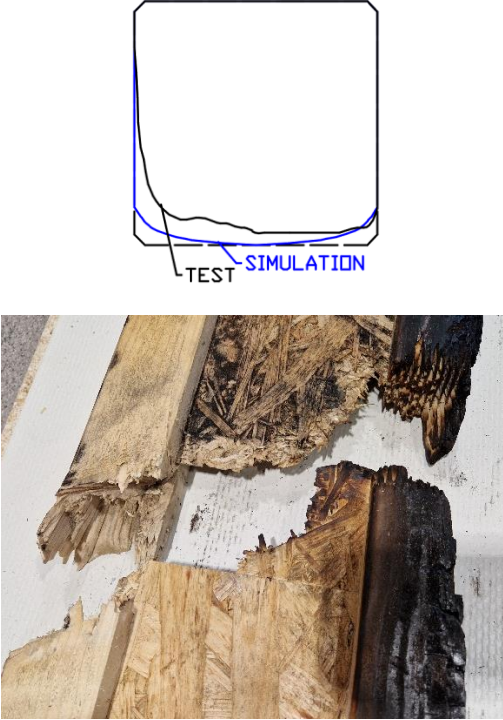


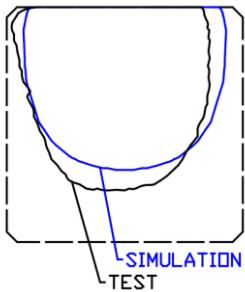
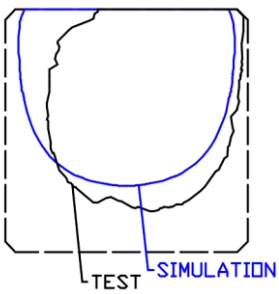
Figure 5.6. The comparison of measured and simulated residual cross-sections for the beams 6.3, 8.3, 9.2 and 12.4.

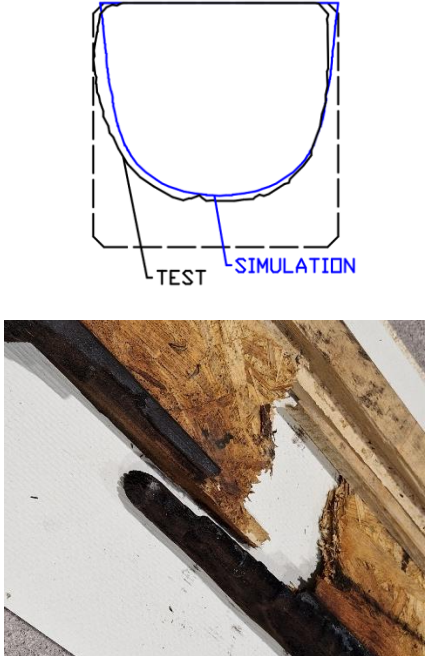
## 5.1 Residual cross-sections of fire exposed flanges

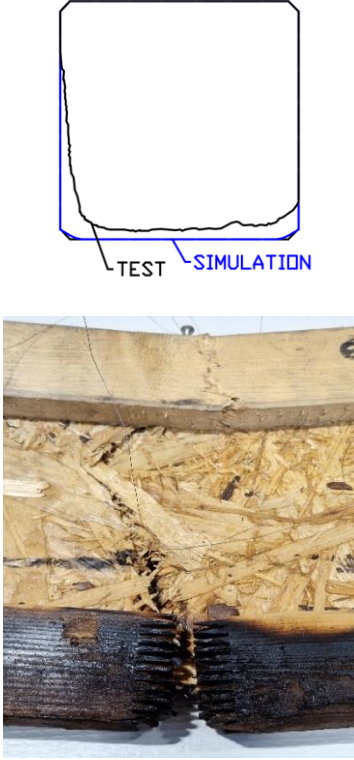
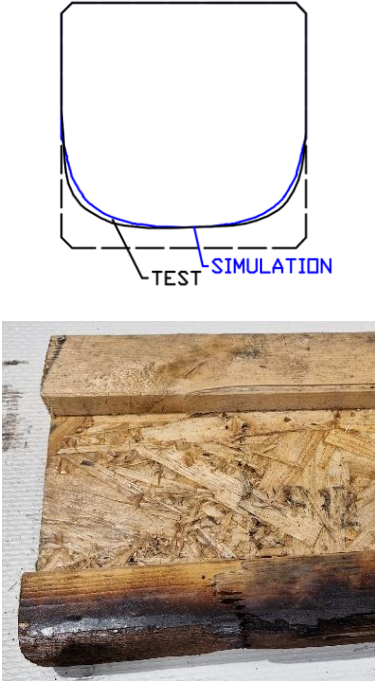
This subchapter examines the charred cross-section contours of various beams remaining after the tests and the corresponding residual cross-sections obtained as a result of the simulation.

Table 2. Analysis of the fire exposed flanges of residual cross-sections.

Residual cross-section of the fire exposed flange and a picture of the location of the failure	Description and analysis
<p style="text-align: center;">1.2</p> 	<p>The contour of the residual cross-section from the simulation is very similar to the actual cross-section measured after the experiment. The simulation can correctly describe the actual course of the experiment.</p> <p>Looking at the photos, it can be seen that the beam failure was caused by the wood breaking at the finger joint.</p>
<p style="text-align: center;">2.2</p> 	<p>The contour obtained as a result of the simulation is somewhat similar to the real one, but on one side of the cross-section, the actual charring depth was much greater than the simulated contour.</p> <p>The difference may come from the difference in temperature rises. The comparison graph of the temperature lines of the simulation and the test shows that the temperature rise between the gypsum and the I-joist in the final stage of the test was much steeper in the actual test than in the simulation.</p> <p>Upon examining the photographs, it is visible that the failure of the beam occurred due to the wood fracturing specifically at the finger joint.</p>

Residual cross-section of the fire exposed flange and a picture of the location of the failure	Description and analysis
<p data-bbox="470 360 531 398">2.4</p>  <p>The diagram shows a cross-section of a beam with a dashed outline representing the original shape. A solid black line represents the 'TEST' result, and a solid blue line represents the 'SIMULATION' result. Both lines show a significant inward curvature at the bottom, indicating deflection. A label 'TEST' points to the black line, and a label 'SIMULATION' points to the blue line.</p>  <p>The photograph shows a physical cross-section of a beam after a fire test. The wood is charred and shows signs of failure, particularly at the bottom flange and the web area.</p>	<p data-bbox="799 304 1378 465">The cross-sectional contours obtained from the test and simulations are quite similar. The simulation describes the course of the experiment correctly and conservatively.</p> <p data-bbox="799 510 1386 801">The flange on the fire side of the beam failed due to wood breakage. However, there is also a visible problem with the effectiveness of the glue, as it is noticeable that the web of the I-joint has come unglued from the non-fire-side flange as a secondary effect due to increased deflections.</p>
<p data-bbox="464 1176 528 1214">3.3</p>  <p>The diagram shows a cross-section of a beam with a dashed outline representing the original shape. A solid black line represents the 'TEST' result, and a solid blue line represents the 'SIMULATION' result. The black line shows a more pronounced inward curvature at the bottom compared to the blue line. A label 'TEST' points to the black line, and a label 'SIMULATION' points to the blue line.</p>  <p>The photograph shows a physical cross-section of a beam after a fire test. The wood is heavily charred and shows significant failure, particularly at the bottom flange and the web area.</p>	<p data-bbox="799 1120 1331 1281">The simulation describes the course of the experiment satisfactorily, but there are still differences with the actual charred cross-section.</p> <p data-bbox="799 1326 1378 1662">The differences can be explained with the comparison graph of the temperature lines. It can be seen from the graph that in the last few hundred seconds before the end of the experiment, the temperatures of the actual experiment reached almost 900 °C, but according to the simulation, the higher temperatures remained slightly above 800 °C.</p> <p data-bbox="799 1706 1267 1778">The beam failure was caused by wood breakage.</p>

Residual cross-section of the fire exposed flange and a picture of the location of the failure	Description and analysis
<p data-bbox="427 331 491 371">6.3</p> 	<p data-bbox="715 304 1385 465">The contour of the residual cross-section from the simulation is very similar to the actual cross-section measured after the experiment. The simulation can correctly describe the actual course of the experiment.</p> <p data-bbox="715 510 1385 846">Based on the photos, it can be said that the fire-side flange failed due to the wood breaking. The glue withstood the test load and there are no noticeable problems with glue resistance in the lower flange. Some longitudinal cracking of wood has also occurred during the test in the fire-side flange. Again, similar to experiment 2.4, it can be noticed that the web has come unglued from the non-fire-side flange.</p>
<p data-bbox="427 1131 491 1171">8.3</p> 	<p data-bbox="715 1104 1385 1350">The cross-sectional contour of the simulation shows much less charring than there actually occurred in the experiment. Looking at the graph of the temperature lines, it can be seen that the lines of the simulations are largely on the safe side. Therefore, the difference cannot be justified by differences in the graph.</p> <p data-bbox="715 1395 1385 1641">From the photos taken of the test object after testing, it is possible to assume that the location of the knot in the fire-side flange played an important role in the failure. It was likely located too close to the finger joint and caused additional stress concentration in the flange.</p> <p data-bbox="715 1686 1385 1809">The simulation describes an average ideal charring. During the actual test, charring, deeper than average has locally occurred at the beam breaking point.</p>

Residual cross-section of the fire exposed flange and a picture of the location of the failure	Description and analysis
<p data-bbox="427 309 488 349">9.2</p> 	<p data-bbox="715 309 1393 510">The simulation underestimated the actual charring. Analysing the temperature graph, it is visible that the temperature lines describe the actual situation conservatively. Therefore, it is necessary to look at the pictures and find the reason for the greater charring.</p> <p data-bbox="715 555 1393 763">The pictures show that the finger joints are quite clean, i.e. the parts of the wood glued together have not visibly stuck to each other, we can conclude that the breakage occurred mainly due to the softening of the glue.</p> <p data-bbox="715 808 1393 1016">There has been localized, deeper than average charring near the failure point. Most likely, the density of the fracture site was lower than the average density of the beam, which caused the failure and greater charring.</p>
<p data-bbox="411 1205 488 1245">12.4</p> 	<p data-bbox="715 1182 1393 1346">The contour of the residual cross-section from the simulation is very similar to the actual cross-section measured after the experiment. The simulation can correctly describe the actual course of the experiment.</p> <p data-bbox="715 1391 1393 1554">The beam failed due to wood breaking in the lower flange on the fire side. The breakage occurred near the finger joint. Some longitudinal cracking is also visible.</p>

The residual cross-sections obtained from the simulations are largely similar to the actual measured cross-sections. In the case of beams 1.2, 2.4, 6.3 and 12.4, the differences are minimal, and based on the simulations, it is possible to correctly describe the temperature and cross-section changes during the test.

In the case of beams 2.2, 3.3, 8.3 and 9.2, it can be seen that the cross-sections obtained during the simulation yields larger charred cross-sections (underestimates char depths). This can be justified by the fact that the simulations describe the average ideal situation of the beam. The simulations are calibrated based on the points where the thermocouples were installed during the experiment. Thus, the simulations describe the average situation of the beam and do not take into account local deeper charring. Wood breakage mostly occurs in areas of lower density where there is also deeper than average charring.

## 5.2 Cross-section comparison tables

Analysing the measured cross-sections comprehensively, summary tables were prepared. The three beams marked in green in the table broke during testing before their fire-side flanges had time to char. Thus, their cross-sections at the end of the experiment were identical to those from the beginning of the experiment.

Table 3 shows the loads used in the test and the resulting properties of the beam: modulus of elasticity, bending strength, compressive stress, tensile stress, bending moment and moment of resistance. Test load ( $F$ ), modulus of elasticity (MOE) and bending strength ( $f_m$ ) values were given in the test report [10].

Table 3. Load-dependent values.

Test beam	Test load $F$ [kN]	MOE [Mpa]	Bending strength $f_m$ [Mpa]	Compressive strength [MPa]	Tensile strength [MPa]	Bending moment [kNm]	Moment of resistance [mm <sup>3</sup> ]
2.2	3.1	12412	35.5	24.41	20.44	4.123	116141
8.3	3.46	13556	39.8	26.11	24.45	4.6018	115623
6.3	3.75	14489	43.4	27.98	27.96	4.9875	114919
5.2	4.08	15564	47.5	29.56	31.97	5.4264	114240
9.2	3.11	12399	35.5	24.4	20.4	4.1363	116515
4.3	3.55	13824	40.9	26.65	25.38	4.7215	115440
11.2	3.6	13995	41.5	26.99	25.98	4.788	115373
3.3	2.41	11301	26.9	21.6	15.7	3.2053	119156
1.2	2.53	11600	28.3	22.4	17	3.3649	118901
7.4	3.01	12930	34.3	24.93	22.26	4.0033	116714

Test beam	Test load $F$ [kN]	MOE [Mpa]	Bending strength $f_m$ [Mpa]	Compressive strength [MPa]	Tensile strength [MPa]	Bending moment [kNm]	Moment of resistance [mm <sup>3</sup> ]
2.4	2.57	11718	28.8	22.87	17.59	3.4181	118684
12.4	3.32	13774	38.1	26.55	25.21	4.4156	115895
11.4	3.1	12410	35.5	24.41	20.44	4.123	116141
8.4	3.1	12410	35.5	24.41	20.44	4.123	116141

The compressive and tensile strengths in the flanges were interpolated by using Table 1 from the standard EVS-EN 338:2016 [14], which describes strength classes for softwood based on edgewise bending tests. For finding the necessary values, the elastic moduli recorded in the experiments were compared and the corresponding compressive and tensile strengths were found.

For the calculation of the bending moment, the leverage of the test beam loads valued as 1.33 meters was taken into account. The leverage can be seen in Figure 3.2. To find the value of the moment, the test load was multiplied by the value of the mentioned leverage. Unit of the bending moment is kNm. Moment of resistance was calculated based on bending moment and bending strength. To find the value, the bending moment was divided by the bending strength, and in order to get the units to match, the value was then multiplied by  $10^6$ . The unit for moment of resistance is mm<sup>3</sup>. The three beams marked in green in the table broke during testing before their fire-side flanges had time to char. Thus, their cross-sections at the end of the experiment were identical to those from the beginning of the experiment.

In Table 4, the measured cross-sections were analysed. Initially at least two values for the area, moment of inertia and centre of gravity location for each cross-section were noted in the table. Afterwards, the necessary average values were calculated, which are presented in the table.

*Table 4. Measured data of charred cross-section.*

Test beam	Average total area $A_{ave}$ [mm <sup>2</sup> ]	Average centroid $y_{c,ave}$ [mm]	Average moment of inertia $I_{ave}$ [mm <sup>4</sup> ]
2.2	5296	97	25953999
8.3	5240.2	96	25430047
6.3	4766.1	86.85	21033710
9.2	5282.9	96.8	25872381
4.3	5478	100	27661034
11.2	5478	100	27661034
3.3	4325.3	78	17424807

Test beam	Average total area $A_{ave}$ [mm <sup>2</sup> ]	Average centroid $y_{c,ave}$ [mm]	Average moment of inertia $I_{ave}$ [mm <sup>4</sup> ]
1.2	4966.8	90.85	22920662
7.4	5478	100	27661034
2.4	4384.8	79.13	17733787
12.4	5173.4	94.65	24736175

As in the previous table the three beams marked in green in the table were uncharred, so their cross-section remained the same as in the beginning. It was not possible to measure the cross-sections of the beams 5.2, 11.4 and 8.4, so they are not reflected in the table.

All the individual values for cross-sectional areas, centres of gravity and moments of inertia were obtained from AutoCAD drawings of the residual cross-sections. Finding the contours of cross-sections for each beam and their further processing is described in Chapter 4.1.

Once the measured data were all available, it was possible to start finding the effective cross-sections for each beam. For this, an attempt was made in Table 5 to find the size of the rectangular flange on the fire side, which would give the centroid and moment of inertia values as close as possible to the real ones. Depending on whether charring occurred only on the fire side of the flange or from three directions, the dimensions of the cross-section were reduced from either only the fire side or both the fire and lateral sides of the fire exposed flange.

Table 5. Calculated data of charred cross-section.

Test beam	$t_{ch,2}$	$b_{fl,1}$ [mm]	$h_{fl,2}$ [mm]	Centroid (measured) [mm]	Centroid (calculated) [mm]	Moment of inertia $I$ (measured) [mm <sup>4</sup> ]	Moment of inertia $I$ (calc) [mm <sup>4</sup> ]
2.2		47	43.55	97	97.00	25953999	26047063
8.3		47	42.42	96	96.00	25430047	25521457
6.3		47	32.53	86.85	86.85	21033710	20967196
9.2		47	43.32	96.80	96.80	25872381	25939969
4.3		47	47	100	100	27661034	27661034
11.2		47	47	100	100	27661034	27661034
3.3	+	27.7	36.64	78	77.45	17424807	17424347
1.2		47	36.75	90.85	90.85	22920662	22902335
7.4		47	47	100	100	27661034	27661034
2.4	+	26.26	38.95	79.13	77.90	17733787	17732010
12.4		47	40.9	94.65	94.65	24736175	24816540

The dimensions of the three beams marked in green did not change during testing. In the cells marked with red colour, values were selected, ensuring that the indicators of the new effective cross-section matched the measured values.

The measured values - centre of gravity and moment of inertia - were taken from Table 4. In the first column  $t_{ch,2}$ , it was determined whether charring occurred from one or three sides in the experiments. Those beams marked with the '+' symbol were charred on three sides, so in their case the effective cross-section had to be reduced from the side facing the fire and also from the lateral sides. Based on this, whether and in how many directions the cross-section decreased, the values of  $b_{fl,1}$  and  $h_{fl,1}$  were further determined. On beams that did not char at all, the effective cross-sections of the fire-side flange remained the original (47x47mm). For beams with charring on only one side, the value of width  $b_{fl,1}$  was kept the same and only the new height  $h_{fl,1}$  was reduced. However, if charring took place on three sides, both dimensions had to be reduced.

When starting to dimension the effective cross-section of the fire exposed flange, the new effective height  $h_{fl,1}$  was first determined, ensuring that the calculated centre of gravity value was as close as possible to the measured centre of gravity. Then the width  $b_{fl,1}$  was determined, which was obtained by observing that the calculated moment of inertia should be as equal as possible to the measured moment of inertia. Since it is not possible to get the moments of inertia to be exactly equal, it was necessary to make sure that the calculated value was slightly lower than the measured one.

In Table 5, the required cross-section dimensions of the fire-side flange of the beam, depending on the comparison of the moments of inertia, were calculated. Table 6 adds one more detail to make the cross-sectional analysis complete. A layer of zero-strength corresponding to each cross-section was found.

Table 6. Data of the effective I-joist cross-section.

Test beam	Test duration [min]	Zero-strength layer $d_0$ [mm]	New cross-section width $b$ [mm]	New cross-section height $h$ [mm]	Centroid from unexposed side $y_c$ [mm]	Distances of the centers of individual beam parts from the center of the entire cross-section			Moment of inertia about the centre of cross-section $I_{tot\_calc}$ [mm <sup>4</sup> ]	Distance from neutral axis to the most extreme fibre $y$ [mm]	Calculated effective moment of resistance $W$ [mm <sup>3</sup> ]	Load dependent moment of resistance $W_R$ [mm <sup>3</sup> ]
						$y_{c1}$	$y_{c2}$	$y_{c3}$				
2.2	26.4	12.94	21.12	30.61	68.12	44.62	31.88	100.19	13413716	115	116145	116141
8.3	26.08	12.73	21.54	29.69	67.87	44.37	32.13	99.98	13281289	115	115666	115623
6.3	38.78	9.98	27.04	22.55	66.54	43.04	33.46	97.74	12528212	109	114923	114919
9.2	24.07	12.84	21.32	30.48	68.19	44.69	31.81	100.05	13438694	115	116568	116515
4.3	22.6	13.75	19.5	33.25	68.39	44.89	31.61	101.24	13614302	118	115508	115440
11.2	12.23	13.76	19.48	33.24	68.36	44.86	31.64	101.26	13604717	118	115414	115373
3.3	32.38	3.56	20.58	33.08	69.20	45.70	30.80	100.34	13934504	117	119222	119156
1.2	29.7	10.83	25.34	25.92	67.99	44.49	32.01	97.97	13198620	111	118982	118901
7.4	15.2	13.62	19.76	33.38	68.69	45.19	31.31	101.00	13739077	118	116735	116714
2.4	24.33	3.51	19.24	35.44	69.43	45.93	30.57	101.29	14116859	119	118622	118684
12.4	29.33	12.33	22.34	28.57	67.74	44.24	32.26	99.54	13193712	114	115908	115895

The dimensions of beams marked with green did not decrease during testing. The values marked in red were found by approximation, ensuring that the resulting moment of resistance was as similar as possible to the value found based on the original loads. It was not possible to take the dimensions of the beams 5.2, 11.4 and 8.4, because they did not arrive from the factory to Estonia for cross-section measurement. Since it was not possible to find a charred cross-section, it was also not possible to calculate the thickness of the zero-strength layer for these beams.

In the first column, the duration of the test is given for each beam. In the following column, the layer with zero-strength was found by approximation by equating different moment of resistance values. The thickness of the zero-strength layer is described in millimetres with an accuracy of 0.01 mm. Columns labelled  $b$  and  $h$  show the final calculated dimensions of the fire-side flange of the beam, where the thicknesses of the zero-strength layer were subtracted from the previously calculated flange dimensions found in Table 5. A single  $d_0$  was subtracted from the height  $h_{fi}$ , and a double  $d_0$  value was subtracted from the width  $b_{fi}$ . Then, for each part of the beam (upper flange, lower flange and the web between them), their moments of inertia and areas were found. Individual values for each different cross-sectional part are not shown in Table 6.

The location of the centre of gravity  $y_c$  was found for the cross-section with new corrected dimensions. According to the newly found centre of gravity, the distance of the centre of each different cross-section part from the centre of gravity of the whole cross-section was calculated. These individual values are also excluded from the general table, but are taken into account in finding the following important values. According to the moments of inertia of the various parts forming the beam, their areas and distances from the centre of gravity, the total moment of inertia of the entire cross-section in relation to the axis passing through the centre of cross-section  $I_{tot,calc}$  was found.

The moment of inertia about the centre of the cross-section in Table 6 was calculated by the formula (5.1):

$$I_{tot,calc} = \sum I_i + A_i * y_i^2 \quad (5.1)$$

where  $I_i$  – moment of inertia of a single part of the I-joist cross-section (upper and lower flanges and the web between them), mm<sup>4</sup>,

$A_i$  – area of individual part of the I-joist cross-section (upper and lower flange and the web between them), mm<sup>2</sup>,

$y_i$  – distance of the centres of gravity of individual parts of the beam cross section (upper and lower flange and web between them) from the centre of gravity of the entire cross section, mm.

Afterwards the distance from neutral axis to the most extreme fibre  $y$  was found. For this, the distances of the centre of gravity from the edges of both flanges were calculated and compared with each other. The maximum value of the two was the determining factor. At that point it was possible to move to the most defining values in this table. In order to find the thickness of the zero-strength layer corresponding to the cross-section of each beam, it was necessary to calculate comparable moment of resistance values. The actual situation was described as the moment of resistance of the cross-section due to the load. The values of this quantity were also shown in Table 3. When calculating the effective moment of resistance, the moment of inertia about the centre of cross-section and the distance from neutral axis to the most extreme fibre were taken into account.

Calculated effective moment of resistance was calculated using the formula (5.2):

$$W = \frac{I_{tot,calc}}{y} \quad (5.2)$$

where  $I_{tot,calc}$  – moment of inertia of the cross-section about the centre of the cross-section, mm<sup>4</sup>,

$y$  – distance from neutral axis of the cross-section to the most extreme fibre, mm.

### 5.3 Results and discussion

In Chapter 5.2 as a result of several measurements and calculations, a zero-strength layer corresponding to each I-joist cross-section was found. The values found range from three to thirteen millimetres. The thicknesses of the zero layer were determined for each beam with an accuracy of 0.01 mm.

The minimum zero-strength layer thickness was obtained for the I-joists marked as 3.3 and 2.4. The corresponding zero-strength layer thickness values were 3.56 mm and 3.51 mm. These beams had the highest charring depth compared to other beams. It can be stated that the relationship is valid, that the thickness of the zero-strength layer is smaller with higher charring. For the beam 3.3, the new effective cross-section dimensions of the fire-side flange of the beam were 20.58 mm and 33.08 mm. Compared to the cross-sectional area of the original fire-side flange, which was 47mm

x 47mm, the new cross-section is approximately 30.8%. Looking at the beam 2.4, it is possible to say that the new cross-section with dimensions of 19.24mm x 35.44mm is approximately 30.9% of the original one.

Next, beams 6.3 and 1.2 were analysed in relation to the determined thickness of the zero-strength layer. The mentioned beams had the following zero-strength layer thicknesses – 9.98 mm for the beam 6.3 and 10.83 mm for the beam 1.2. Looking at chapter 5.1, where different residual cross-sections were presented, it can be seen that for both beams the contours of the simulation and the actual cross-section were very similar. Charring occurred mainly on one side on both beams. Charring was not as deep as on beams 2.4 and 3.3, which were analysed previously. Again, proof of the relationship can be seen that as the charring depth decreases, the thickness of the zero-strength layer increases. The new fire-side flange cross-sections were found to be 27.04mm x 22.55mm for beam 6.3 and 25.34mm x 25.92mm for beam 1.2, which make up 27.6% and 29.7% of the original flange cross-section, respectively.

The values of the zero-strength layer found for the seven beams left to be analysed - 2.2, 8.3, 9.2, 4.3, 11.2, 7.4 and 12.4, are quite equivalent. They all vary between 12 and 13 millimetres. Based on the cross-section contours of the remaining beams, it can be seen that the charring depth is much lower compared to the previously analysed beams. In the case of beams 3.3, 2.4, 6.3 and 1.2, it was mentioned that the similarity of the residual cross-sections obtained as a result of the simulations were very similar to the actual measured cross-sections. While the charring of the present test specimens was much smaller, the differences are also much larger. The simulations are no longer able to describe the local charring situation as accurately. In the case of beam 12.4, it was still possible to accurately describe the remaining cross-section after the fire test with simulation. However, in the case of other beams, on which a certain, but in this case rather small, charring occurred, it can be noticed that the simulations underestimated the local charring at the point of failure and could not conservatively describe the situation at that point. Visible charring was minimal for beams 4.3, 11.2 and 7.4, so the cross-sections did not change during testing.

On beams whose cross-section did not change during testing - 4.3, 11.2 and 7.4, the thicknesses of the layer with zero strength were found to be 13.75 mm, 13.76 mm and 13.62 mm, respectively. The thickness of the zero-strength layer is the largest on these beams. The minimum charring is accompanied by the maximum thickness of the zero-strength layer. After subtracting the zero-strength layer the new cross-sections make up 29.4% of beam 4.3, 29.3% of beam 11.2 and 29.9% of beam 7.4 of the original cross-section of 47mm x 47mm. Since the loads and the dimensions of the cross-

sections were the same for these beams, it is possible to justify the similar results. The only difference was the glue used for these test specimens, and various local defects can always play a role, which can weaken the beam.

For beams 2.2, 8.3, 9.2 and 12.4, the values of the zero-strength layer were found to be 12.94 mm, 12.73 mm, 12.84 mm and 12.33 mm. This makes the new effective fire side flange cross-section dimensions on beam 2.2 29.2%, beam 8.3 29.0%, beam 9.2 29.4% and beam 12.4 28.9% of the original fire side flange cross section 47mm x 47mm.

For beams 5.2, 11.4 and 8.4, it was not possible to find the thickness of the zero-strength layer, because during the work, it was not possible to determine the cross-section dimensions of these beams. Cross-section measurements after the test were carried out in Estonia. The mentioned three beams did not arrive in Estonia from the factory, where the tests were carried out.

The values of the zero-strength layer are satisfactory and follow the principle stated in the work that the greater the charring depth of the wood, the smaller the thickness of the zero-strength layer.

## **SUMMARY**

I-joists have emerged as a viable alternative to traditional wooden frames in modern construction. Their unique design offers several benefits. However, fire safety remains a critical concern in larger and taller timber buildings, especially when forming load-bearing timber frame structures with I-joists. This thesis aims to address this gap by modelling the fire behaviour of I-joists through finite element thermal simulations and comparing the results with actual test outcomes.

The research objective is to achieve a high level of similarity between the simulation results and the test findings. The thermal simulations take into account not only the behaviour of the I-joists themselves but also the existing fire protection system, including gypsum board and cavity insulation, as well as the timing of plasterboard fall-off. Additionally, the determination of the zero-strength layer corresponding to each I-joist through cross-section measurements and various calculations adds valuable insights to the study.

By conducting loaded model scale tests and carrying out thermal simulations, the thesis aims to provide a comprehensive understanding of the fire resistance of load-bearing timber frame structures utilizing I-joists. The comparison between experimental results and simulation outcomes will enable researchers, architects, and engineers to make more informed decisions regarding fire safety measures in timber constructions.

This thesis contributes to the advancement of fire safety knowledge in timber buildings by exploring the behaviour of I-joists through a combination of experimental testing and thermal simulations. The findings and conclusions drawn from this research will play a crucial role in enhancing the design and construction practices of tall timber buildings, ensuring their long-term sustainability and safety as a construction solution for the future.

## KOKKUVÕTE

I-talad on tänapäeva ehituses kujunenud arvestatavaks alternatiiviks traditsioonilisele puikarkassile. Nende ainulaadne disain pakub mitmeid eeliseid. Suuremate ja kõrgemate puitehitiste puhul jääb tuleohutus siiski kriitiliseks probleemiks, eriti I-taladega kandvate puikarkasskonstruktsioonide moodustamisel. Selle lõputöö eesmärk on anda panus lahendamaks antud puudujääki, modelleerides I-talade tulekäitumist lõplike elementide termiliste simulatsioonide abil ja võrreldes tulemusi tegelike katsetulemustega.

Uurimise eesmärk on saada simulatsiooni tulemused võimalikult sarnased võrreldes tegelike katsetulemustega. Termosimulatsioonid ei võta arvesse mitte ainult I-talade endi käitumist, vaid ka erinevaid kaitsvaid elemente, sealhulgas kipsplaati, talade vahelist isolatsiooni ning kipsplaadi mahakukkumise aega. Lisaks lisab uuringule väärtuslikku teavet igale I-talale vastava nulltugevuse kihi määramine ristlõike mõõtmiste ja erinevate arvutuste abil.

Lõputöö eesmärk on koormatud katsetuste ja termosimulatsioonide läbiviimise kaudu anda edasi terviklik arusaam I-talade kasutatavate kandvate puikarkasskonstruktsioonide tulepüsivustest. Katsetulemuste ja simulatsioonitulemuste võrdlus võimaldab teadlastel, arhitektidel ja inseneridel teha teadlikemaid otsuseid puitkonstruktsioonide tuleohutusmeetmete kohta.

Antud lõputöö aitab kaasa tuleohutusosalaste teadmiste edendamisele puithoonetes, uurides I-talade käitumist eksperimentaalsete katsete ja termiliste simulatsioonide kombinatsiooni kaudu. Selle uuringu tulemused ja järeldused mängivad otsustavat rolli kõrgete puithoonete projekteerimis- ja ehitustavade täiustamisel, tagades nende pikaajalise jätkusuutlikkuse ja ohutuse tuleviku ehituslahendusena.

## LIST OF REFERENCES

- [1] *The I-joist Handbook by Masonite Beams*. 2022.
- [2] K. N. Mäger and A. Just, 'Preliminary design model for wooden I-joists in fire', in *Proceedings of 52nd meeting of International Network on Timber Engineering Research*, Tacoma, USA, 2019.
- [3] K. N. Mäger, 'Design Methods for Wood-Based I- Joists Exposed to Fire – State-of-the-Art and Improvements', 2018.
- [4] CEN, 'EN 1995-1-2:2004. Eurocode 5: Design of timber structures - Part 1-2: General - Structural fire design'.
- [5] A. I. Bartlett, R. M. Hadden, and L. A. Bisby, 'A Review of Factors Affecting the Burning Behaviour of Wood for Application to Tall Timber Construction', *Fire Technol*, vol. 55, no. 1, pp. 1–49, Jan. 2019, doi: 10.1007/s10694-018-0787-y.
- [6] K. N. Mäger, M. Tiso, and A. Just, 'Fire Design Model for Timber Frame Assemblies with Rectangular and I-Shaped Members', in *Wood & Fire Safety*, L. Makovicka Osvaldova, F. Markert, and S. L. Zelinka, Eds., Cham: Springer International Publishing, 2020, pp. 268–274. doi: 10.1007/978-3-030-41235-7\_40.
- [7] M. Tiso, *The contribution of cavity insulations to the load-bearing capacity of timber frame assemblies exposed to fire*. Tallinn: TTÜ Press, 2018.
- [8] K. N. Mäger, 'Influence of Adhesives on Fire Resistance of Wooden I- Joists', 2020.
- [9] J. Schmid, M. Klippel, A. Just, and A. Frangi, 'Review and analysis of fire resistance tests of timber members in bending, tension and compression with respect to the Reduced Cross-Section Method', *Fire Safety Journal*, vol. 68, pp. 81–99, Aug. 2014, doi: 10.1016/j.firesaf.2014.05.006.
- [10] A. Just, R. Olofsson, K. N. Mäger, and M. Sterley, 'D 3.2 Loaded fire tests with I-joists', 2021.
- [11] 'SAFIR', Jan. 17, 2023. [https://www.uee.uliege.be/cms/c\\_6331644/en/safir](https://www.uee.uliege.be/cms/c_6331644/en/safir) (accessed Jan. 17, 2023).
- [12] J.-M. Franssen and T. Gernay, 'Modeling structures in fire with SAFIR®: theoretical background and capabilities', *Journal of Structural Fire Engineering*, vol. 8, no. 3, Art. no. 3, Jan. 2017, doi: 10.1108/JSFE-07-2016-0010.
- [13] B. Östman, Ed., *Fire safety in timber buildings: Technical guideline for Europe*. SP Technical Research Institute of Sweden, 2010.
- [14] EVS, 'EVS-EN 338:2016 Structural timber - Strength classes'.